The University Of Sheffield.

Formation and Propagation of Collisionless shock wave in Earth Magnetosphere

by

Jivraj Pipaliya

A thesis submitted in partial fulfilment of the requirements for the degree of

Master of Philosophy

The University of Sheffield

Faculty of Engineering

Department of Automatic Control and Systems Engineering

May 18, 2018

Acknowledgements

I am thankful to Cluster Active Archive (CAA) of the European Space Agency (ESA) and National Research and Development Agency, UK Space Agency, NASA, Japan Aerospace Exploration Agency (JAXA) for the data provided.

Contents

1 Introduction

One of the key aspects of the in-situ measurements of Collisionless Shocks (CS) is to identify direction of the wave propagation and shock normal variation in the Earth magnetopause. Second aspect is related to the identification of the Quasi Perpendicular Shock (QPS) parameters such as variation of the the angle between shock normal and upstream magnetic field θ_{Bn}, magnetic field variation in Earth Magnetic ramp $\frac{\delta B}{B_0}$ region and Mach number. This is important because at various planetary missions plasma parameters and magnetic field data are not available. High energetic plasma particles radiate from Sun's surface into inter planetary space. The high speed solar wind plasma (approximately 400 to 600 km/s) contains ions, electrons, electro-static and electro-magnetic waves which interact with inter-planetary and resistive Earth magnetic field. The interaction between energetic plasma particles and resistive magnetic field form the plasma shock structures around planets (and Earth) at the boundary of the incoming solar-wind transients.

Colliding inter-stellar winds around supernova remnant resulted from Gamma ray burst radiates high energetic particles i.e. electrons, electron neutrinos, electron muons, electron tao, ions plasma particles and induce high energetic non-stationary inter planetary CS. Such a structure around the Earth's is known as a Earth bow shock which appears at distance $15.23R_E$ up to $13.67R_E$ from the Earth.

Understanding of CS structure is important for many aspects of space physics, astrophysics, fundamental plasma physics and technology, see e.g. (Balikhin, 2014, Bale, 2005, Fujimoto & Phan & Toth, 2015). In particular, CSs accelerate ion-electron plasma charge particles to very high speed (Wilson, 2016) which interact with solar-wind, Earth magnetic field and participate in formation of tilted magnetosphere in Sun-Earth line direction (Fujimoto & Phan & Toth, 2015, Kajita, 2017, Russell et. al., 2007). The formation of the Earth magnetosphere and classification of its regions is

discussed in Chapter 2 of this work and previously in a number of papers e.g. (Bale, 2005, Burch et al., 2016, Fujimoto & Phan & Toth, 2015, Marcowith, 2016, Russell, 2016a). The structure of CS explained in details in Chapter 3.

1.1 Objectives

CS is the simplest configuration where the macroscopic motion can be controlled by the dissipation, and therefore, the understanding of physics and space science and technology of such a process can be applied to the various plasma and magnetic field processes, for example for inter planetary space magnetic field and laboratory plasma. The main point is that CS wave energy transition is responsible for ion and electron charged particles acceleration.They are ubiquitous in the universe, for example, CS are form around planets in the heliosphere, at the boundaries of the solar wind transients, around ordinary stars, in the colliding stellar winds of binary systems, around supernova remnants, result from Gamma Ray Bursts (GRB) and in the vicinity of many other remote astrophysical objects. CS can be subjected to the in-situ measurements are shocks in the heliosphere. The modification of the shock type is known for the relatively low Mach numbers from subcritical dispersive/resistive shocks below critical whistler and first critical Mach number, viscous shocks between the first and the second critical Mach numbers, stationary reflection shocks above the second critical Mach number and finally non-stationary shocks above shock called the third critical Mach number. It is also known that CS with high Mach numbers associated with GRB differs significantly in structure and represent themselves unmagnetised shocks mediated by the filamentary instability. The identification of plasma parameters based on their dependence on shock magnetic field. Objectives of this research work are following:

- Analyse the FGM measurement taken during crossing of Cluster C1, C2, C3, C4 satellites of the Earth bow shock.
- Analysis of QPS structure formation in sunward Earth direction between 10.05 and 8.67 R_E and comparison with Cluster PPSNS real time measurements;
- Analysis of the shock normal variation $\frac{\delta B}{B_0}$ at the QPS front;

- Shock normal measurements;
- Calculation of the angle variation between the shock normal and upstream magnetic field θ_{Bn} at QPS;
- Analysis of the HIA data of the density n_e, 3D particles radial motion v_x, v_y, v_z, ions pressure $P_{i\|}$, electron plasma pressure $P_{e\perp}$, ion parallel $T_{i\|}$ and electron plasma perpendicular $T_{e\perp}$ temperatures, and energy variation;
- Shock normal v_n and Alfvén velocities v_A variation at the magnetic ramp and calculation of the Mach number (M) variation;.
- Calculation of the angle between shock normal and upstream magnetic field θ_{Bn} and validation of obtained results with theoretical Paredu method;
- Classification of QPS measured parameters i.e. $\frac{\delta B}{B_0}$, θ_{Bn}, Mach number M.

1.2 Classification of shocks

A different types of shock structures can be classified by the value of Mach numbers i.e.

- Shocks with a low Mach number;
- Low Mach hydro-dynamic shock $0.3 < M < 0.8$ (sub sonic speed 512 km/s);
- Mach number $0.8 < M < 1.2$ (sound speed 610 up to 915 km/s);
- Mach number $1.2 < M < 5$ (corresponding sound speed 915 up to 3840 km/s);
- Mach number shock $5 < M < 10$ (hypersonic speed 3840 km/s up to 7680 km/s);
- Very high Mach number $10 < M < 25$ (high hypersonic speed 16000 km/s).

CS front structure forms due to reflection, deflection of ions by Lorentz force, i.e. $-q_e(\mathbf{v}\times\mathbf{B})_x$. Here $\mathbf{v}$ is the velocity of the electron plasma particles, $\mathbf{B}$ is magnetic field (Stone & Tsurutani, 1985). Hypersonic plasma flow de-accelerate to subsonic speed in collisionless magnetised plasma. The ions reflection beam, speed of longitudinal wave resulted from mass of ions and pressure of the electromagnetic field (EMF) is fluctuating down stream magnetic field and provide main energy. The ion down stream reflection from resistive magnetic field induce energy dissipation at critical Alfvén Mach number (M_A) and low Mach plasma due to Lorentz force. CS structure formed in magnetise plasma depends on the first critical Mach number i.e.:

$$M_{f1} = \frac{C_s}{v_A},$$

Critical Mach number M_f classified for inter planetary space CS, see e.g. (Balikhin et al., 2002, Edmision, 1984, Hobara et al., 2010). Ions energy scattering measurements by CIS instrument on board of C1-C4 is provided Chapter 3. Ion-electron plasma particles density perturbation n_i and n_e induces temperature $T_{i\|}$, $T_{e\perp}$ variation in magnetic ramp $\frac{\delta B}{B_0}$ region and as a result changes ion-sound speed, whistler wave speed, plasma particles speed which can be detected by PPSNS on board HIA (see Chapter 3 for more details).

An ion-ion instability compress magnetic field lines and induce magnetic field turbulence. Magnetic field variation appears at the shock front within in planetary magnetosphere (i.e. Earth, Mercury, Jupiter, Saturn, Uranus, Neptune). Shock wave compress magnetic field and induces magnetic turbulence at high magnetic Reynolds number $100 \leq R_M \leq 200$. Turbulent and elliptically polarised magnetic field and density n_e variation at the magnetic ramp $\frac{\delta B}{B_0}$ transition region induce Alfvén velocity:

$$v_A = \frac{|B|}{\sqrt{4\pi n_e m_e}}$$

Here, $|B|$ is the magnetic field strength, n_e is the electron plasma particles density, m_e is the electron plasma particles mass. The Alfvén speed changes with time due to ions, electron plasma particles density n_i, n_e and magnetic field variation.

1.3 Critical Mach Number of Collisionless Shocks classification

The shocks can be divided into three different types:

- The sub-critical dispersive/resistive shocks below the critical whistler and first critical Mach number;
- Viscous shocks between the first and second critical Mach numbers;
- Non-stationary kinetic shocks at third critical Mach numbers.

CS with high Mach numbers are usually associated with Gamma ray bursts. They are different in structure from unmagnetised shocks generated by filamentary instability, see e.g. (Caprioli & Spitkovsky, 2013). In space plasma the quantitative changes in shock structure can be identified by various parameters. For example, by analysing ion or electron plasma particles density n_i, n_e, pressure $P_{i\|}$, $P_{e\perp}$, temperature of ions and electrons $T_{i\|}$, $T_{e\perp}$, particles velocities v_x, v_y, v_z, electric and magnetic fields.

Determination of the scale of perpendicular and parallel components of the electric and magnetic fields at the ramp region of CS (see Figure 1) in short time scale is an important problem of physics of CS (Bale, 2005, Burch et al., 2016, Russell, 2016a). In certain condition CS shows a non stationary quasi periodic dynamics which is related to the gradient, i.e. scale of the magnetic ramp $\frac{\delta B}{B_0}$ region and whistler wave form

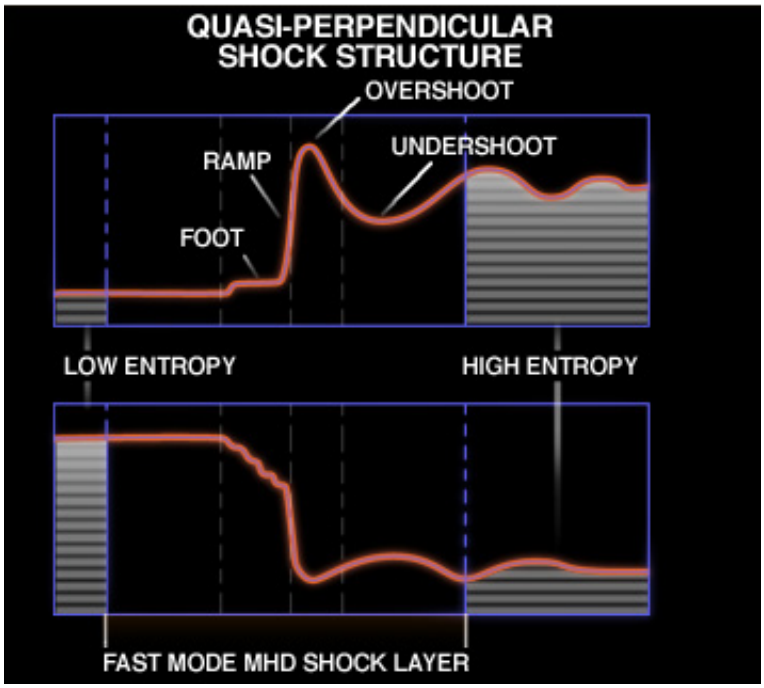

Figure 1: The structure of the Quasi perpendicular shock (QPS). The foot, ramp, overshoot, undershoot regions of the QPS are shown (courtesy to `http://spacephysics.ucr.edu/index.php?content=solar_wind/proc/p2.html`).

precursor wave train. Magnetic field in ramp region depends on the spatial scales of the Quasi Perpendicular Shock (QPS).

A drifting shock acceleration (DSA) form shock potential and partial diffusion shock acceleration which can be evaluated within finite values of the following parameters:

$$\frac{c}{\omega_{pe}} = \sqrt{\frac{4\pi q_e^2 n_e}{m_e}},$$
$$\frac{c}{\omega_{pi}} = \sqrt{\frac{4\pi q_i^2 n_i}{m_i}},$$
$$\lambda_{De} = \sqrt{\frac{k_B T_{e\perp}}{4\pi n_e^2}}.$$

Here ω_{pe} is the electron plasma gyration frequency, ω_{pi} is the ion plasma frequency, λ_{De} is the Debye length, c is the speed of light, q_e is the electric charge, n_e is the

density of electrons and ions density n_i, m_e are the mass of electrons and ions, $T_{e\perp}$ is the temperature of the electron plasma particles, k_B is Boltzmann's constant (Sironi & Spitkovsky, 2009). The Debye length (λ_{De}) is the scale over which initial electric field E_0, and electric field are screened out by the electrons redistribution (Bale et al., 2003, Krasnoselskikh et al., 2013). A dynamic behaviour of the magnetic ramp structure of the QPS can be measured by instrumentation on board of Cluster C1-C4 satellites. The three dimensional Fluxgate Magnetometer (FGM), for example, provides the high time-resolution measurements of three components of the magnetic field B_x, B_y, B_z.

Further details on magnetic field components measurements, methods of analysis and estimations at the ramp region are discussed in Chapter 3, Subsection 3.2.1.

The measurements of the electron plasma particles motion at the ramp region of QPS front by HIA are discussed in Chapter 3. The results of analysis of data obtained on board of PPSNS validated by numerical calculation i.e. magnetic field variables real time PPS measurement by MVA method explained in Chapter 4. FGM magnetic field data analysis performed within finite magnetic-field ramp transition region scale (Bale et al., 2003, Hobara et al., 2010). i.e.

$$L_e = \frac{B_{max} - B_{min}}{|B_0|}.$$

My approach is to detect Mach number (M) of the CS, QPS and its formation in the heliosphere. On that bases detect magnetic field and plasma parameters processes in ramp transition region. Quasi parallel shock formation in sunward Earth direction at radial distance 10.02 R_E magnetosheath and formation of the QPS at $10.05R_E$ Earth magnetopause are discussed in Chapter 2. The magnetosphere subdomain region polarisation and QPS formation at the sunward Earth radial distance $8.42R_E$ up to 15.05 R_E explained further in Chapter 2, Subsection 2.1.

1.4 Summary

Different types of shock formation identified within Mach number limit can be classified as:

- (i) Low Mach shock structure formation, for example, on aircraft wing surface layer and air craft engine;
- (ii) Critical Mach limiter MHD shock in planetary space domain region;
- (iii) Very high Mach$\simeq$ 40 limiter Pulsar shock formation in galaxy, nutron star;
- (iv) Sub Critical Mach Collisionless shock formation in Venus;
- (v) Quasi Parallel shock and Quasi Perpendicular shock (QPS), High Mach limiter non stationary Quasi Perpendicular Shock structure formation in planetary magnetic field i.e. Earth, Jupiter, Neptune, Mercury, Saturn.

The Earth magnetosphere subdomain and shock formation discussed further in Chapter 2. CS, Earth bow shock potential and QPS structure formation at sunward Earth radial distance $8.43R_E$ up to $15.23R_E$ Earth magnetopause are presented in Chapter 2, Subsection 2.1. Quasi Parallel shock formation at $10.04R_E$ Earth magnetosheath region further detail is explained in Chapter 2.

2 Earth Magnetosphere

Magnetic field topology in magnetised Earth plasma is created by interaction of continuous solar wind and Earth magnetic field (Anderson, 1966, Fujimoto & Phan & Toth, 2015). This region can be classified as following:

- Magnetopause;
- Magnetosheath;
- Open magnetopause;
- Magnetotail;
- Plasma-sheet region;
- Neutral sheet.

The general structure of the the Earth magnetosphere is shown in Figure 2. Magnetic field line induced from inner Earth core (Jackson, 2014). South-north magnetic field lines L_1, L_2, , , L_{n-1}, L_n surrounding the Earth form the magnetosphere surface (Fujimoto & Phan & Toth, 2015). Solar wind plasma particles pressure on the Earth magnetic dipole field B_0 with time at equatorial plane and compress resistive Earth magnetopause transition region and induce 1^{st} and 2^{nd} order of perturbation, see e.g. (Hu & Bengt, 2003). The Earth magnetic field reduces the influence of highly energetic cosmic ray, ion and electron plasma particles in sunward side. Incoming solar wind plasma compress the Earth magnetic-field at approximately 65000 km in sun-ward direction as shown in Figure 3. Solarwind plasma particles pressure P_{sw} to the Earth magnetic field pressure P_B induce shock potential barrier. Shock front changes magnetic field and magnetic field compression rate increased with density level of the ions plasma particles (n_i).

A ratio of solar wind plasma pressure P_{sw} to the magnetic field pressure P_M is known as plasma-β. i.e.

$$\beta = \frac{8\pi(n_e \pm n_i)k_B(T_{i\parallel} \pm T_{e\perp})}{B^2}. \tag{1}$$

Here n_e is electron density, B is magnetic field magnitude, k_B is Boltzmann constant, $T_{e\perp}$ is the temperature of the electron plasma particles, $T_{i\parallel}$ is ions plasma particles temperature. The Earth bow shock structure is characterised by ions and electron plasma particles magnetisation (σ) (Sironi & Spitkovsky, 2009) i.e.

$$\sigma = \frac{\omega_c^2}{\omega_p^2} = \frac{B^2}{4\pi\gamma(n_i \pm n_e)(m_i + m_e)c^2}. \tag{2}$$

The magnetic field and incoming solar-wind plasma particles induce the Earth bow shock in sun-earth direction at 97000 km e.g. $15.23R_E$ (Wilson, 2013). The kinetic plasma pressure P_{sw} and magnetic pressure P_M form at interactive surface feature boundary shock potential barrier. Ion and electron plasma particles decouples form IMF at Earth bow shock front. Earth magnetic dipole field and IMF separated in front of the Earth bow shock. Shock wave energise ion and electron plasma particle fluxes and, therefore, changes the Earth magnetic field dipole geometry. Shock wave dispersion is transform diffuse EMF energy into ions, electron particles. Ion and electron plasma energy related to the wave heating in Interplanetary Magnetic Field (IMF), Earth magnetic field reconnection region. Also, it results in increasing of electric field and electron plasma density n_e fluctuation (Balikhin, 2014, Bale, 2005, Fujimoto & Phan & Toth, 2015, Wilson, 2016). If in case of a small variation the large 1^{st} and 2^{nd} order perturbation influenced on ions plasma particles density (n_i) and electron plasma particles density (n_e).

At each point the parallel ions pressure $P_{i\parallel}$ and perpendicular electron plasma pressure $P_{e\perp}$ oscillation (i.e. $P_{e\perp} \pm P_{i\parallel}$) induce 1^{st} and 2^{nd} order perturbation in compress

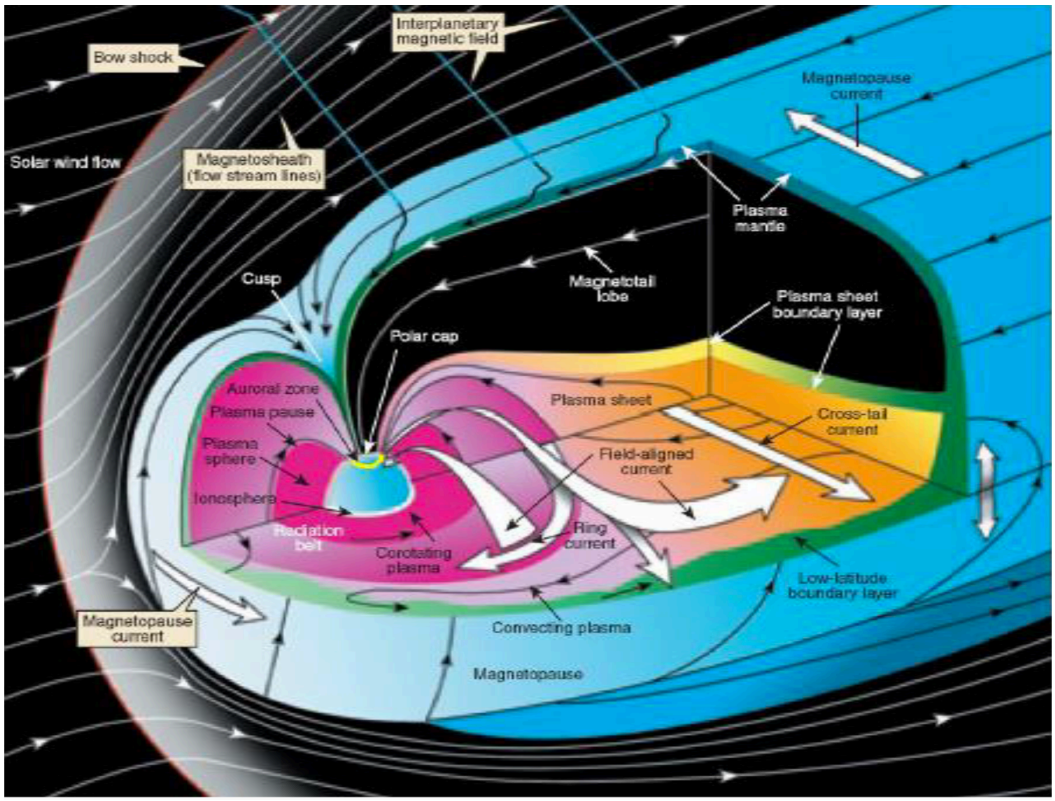

Figure 2: The structure of the Earth's magnetosphere. The following regions are shown: solar wind, bow shock, interplanetary magnetic field (IMF), magnetopause, magnetopause current, magnetosheath, open magnetopause and cusp region (courtesy to ESA).

magnetic field form shock due to $\mathbf{v} \times \mathbf{B}$ force. The plasma wave propagation at this region is distorted due to large amplitude magnetic fluctuation known as shocklet, i.e. small shocks (Stone & Tsurutani, 1985, Wilson, 2013b). Additionally, the shock wave energise magnetised electron plasma and heat shock plasma ions in normal angle θ_{Bn} to Earth magnetic field. A down stream ions internal energy density flow to upstream electron internal energy density flow ratio are differ at each transition state space domain point. The upstream direction gyro-radial electron plasma motion induces across magnetic field lines in gyration mode. The heavy ions reflection/deflection occurs in down stream region due to $\mathbf{v} \times \mathbf{B}$ force.

The ions reflected from compressed magnetic field provides energy for precursor excitation, i.e. whistler wave. Therefore, the small 1^{st} order perturbation in electro static potential lead to the large variation into down stream ions internal energy density flow and upstream gyrating electron internal energy density flow. If velocity of plasma particles is close to the wave phase speed (v_{ph}) of the electromagnetic wave, the wave-particle energy exchange is effective. Due to the ions reflection from the shock, the various types of instabilities occur in this region. For example, ion-ion instability, electron-ions instability, electron-electron upstream instability can be excited due to the inter collision, self generated magnetic field in CS (Sironi & Spitkovsky, 2009). The dissipation and dispersion of the propagating shock wave acceleration and energy transform in the shock ramp region can be studies in the framework of Quasi Perpendicular Shock theory.

2.1 Magnetopause

A boundary surface between incoming solar wind ions, electrons and Earth magnetic field in sunward side is known as Earth magnetopause (Russell et. al., 1998a). This region is formed at Earth radial distance $10.05R_E$ in sun-earth direction of the magne-

tosphere (Fujimoto & Phan & Toth, 2015, Russell et. al., 1999, Wilson, 2013). Polarisation of the magnetopause can be classified into three different ways (Russell et. al., 1999):

- Circular magnetopause polarisation;
- Elliptical magnetopause polarisation;
- Planar magnetopause polarisation.

Solar wind plasma particles pressure P_{sw} changes at upstream magnetic field to wave propagation angle θ_{Bk}, as the Earth magnetic dipole field distance B_{DC} variation occurs in horizontal direction at equatorial plane in inhomogeneous magnetic field line B_0 surface (Browning, 2005, Russell et. al., 1998a).

2.1.1 The effect of Earth bow shock potential on plasma particles

The Earth magnetopause magnetic field pressure P_M perturbation is different in comparison to the plasma pressure P_{SW} and induce the Earth bow shock potential barrier (Fujimoto & Phan & Toth, 2015, Russell et. al., 1999). The variation of the Earth bow shock width (i.e 200 km up to 300 km) appears at 15.0 R_E as shown in Figure 3 (Fujimoto & Phan & Toth, 2015). Ions plasma particles propagate in parallel direction to the initial inhomogeneous magnetic field B_0. Thermalised ions and fluctuation of ions reflect back into downstream from sunward Earth magnetopause resistive magnetic field boundary surface. Ions plasma particles density perturbation n_i compress Earth magnetopause downstream magnetic field surface and induces foot region of the QPS. As a result, the fraction of the ion kinetic energy dissipates on shock wave surface. At the same time, the shock wave compress upstream electron plasma particles density n_e and resistive magnetic field into the Earth magnetopause transition region (Farris & Russell, 1993).

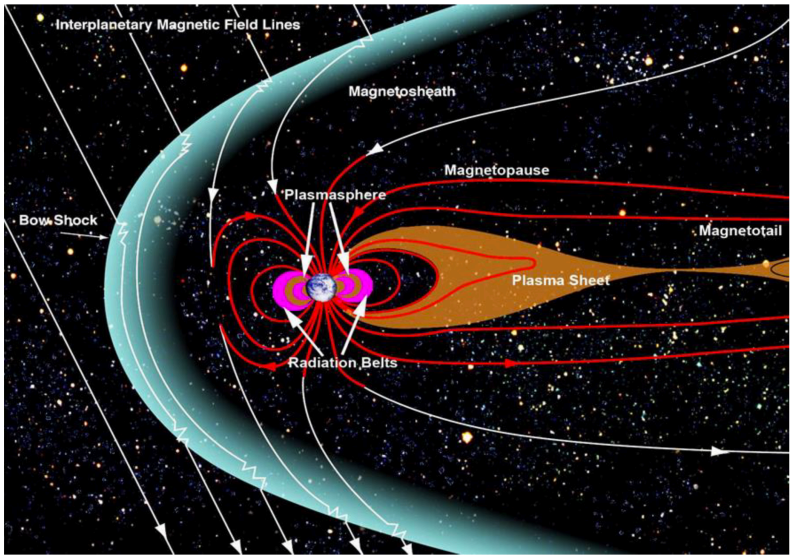

Figure 3: Earth bow shock structure at radial distance 15.23 R_E is shown in blue colour. Magnetic field lines are shown in red colour. Radiation belt A at 12000 km and B at 4000 km are shown in pink. Magnetotail and plasma sheet region are shown in dark yellow colour (courtesy to ESA/NASA).

The ion plasma particles pressure $P_{i\|}$, $P_{\perp}$ variation on resistive Earth magnetic surface induce turbulently elliptically polarised B_x, B_y, B_z at the ramp transition region of the QPS front. Elliptically polarised upstream electron plasma density n_e variation induces dynamic perpendicular pressure $P_{e\perp}$ at $10.05R_E$ (Balikhin, 2014, Bale, 2005, Merka, 2003).

Reflective ion particles density n_i changes in downstream at ramp $\frac{\delta B}{B_0}$ region of QPS front. As a result, thermal ions induce dynamic perpendicular pressure $P_{e\perp}$ on resistive Earth magnetic field line boundary surface at ramp. Clockwise ion cyclotron radial motion i.e. ions kinetic energy transforms into thermal energy and dissipates on shock wave surface. The electron plasma charge particles turbulence flow polarised in velocity space v_x, v_y, v_z and cross coupled with B_x, B_y, B_z surface at the ramp region. It induces a wave propagation changes in each angle between wave propagation and upstream magnetic field.

2.1.2 Interplanetary Magnetic Field (IMF) and it's influence on plasma particles motion

Interplanetary Magnetic Field (IMF) controls solar wind ions and electrons plasma interaction rates at sunward Earth $8.76R_E$ to $10.05R_E$ region (Burch et al., 2016, Morner, 2013). Each magnetic moment of inertia changes on unpolarised B_0 surface at equatorial plane. Ion parallel pressure $P_{i\|}$ and electron perpendicular pressure $P_{e\perp}$ on initial unpolarised magnetic field B_0 surface partially diffuses magnetic energy. As a result, electron plasma particles temperature $T_{\|}$ variation occurs on B_0 surface (Carolus, 2009).

Earth magnetopause resistive magnetic field transition region induces magnetic field and e-plasma turbulence. At the front of Earth magnetic dipole field distance B_{DC} variation induce 1^{st} order perturbation classified as a time varying initial horizontal directional inhomogeneous magnetic field B_0 surface vibration, translation and LHS and RHS circularly polarised ions plasma particles parallel motion $v_{i\|}$ at low magnetic Reynolds number $0 < R_M \leq 100$. Circularly LHS polarised gyrating ions parallel pressure $P_{i\|}$ on unpolarised magnetic field line B_0 surface partially diffusive magnetic energy variation occurs in all directions (Burch et al., 2016, Wilson et.al., 2014).

2.2 Magnetosheath

The region between Earth magnetopause and Earth bow shock is known as magnetosheath is shown in Figure 4. Earth bow shock strengthen supersonic solar wind particles from the magnetosheath in sunward side magnetosphere (Fujimoto & Phan & Toth, 2015). Earth magnetic dipole field surface is elliptically polarised to initial unperturbed horizontal magnetic field B_0 in the right or left hand direction (Anderson, 1966, Russell et. al., 1998a). Magnetic energy density fluctuation in all directions perpendicular to the initial unperturbed magnetic field (B_0) surface at lower latitude boundary

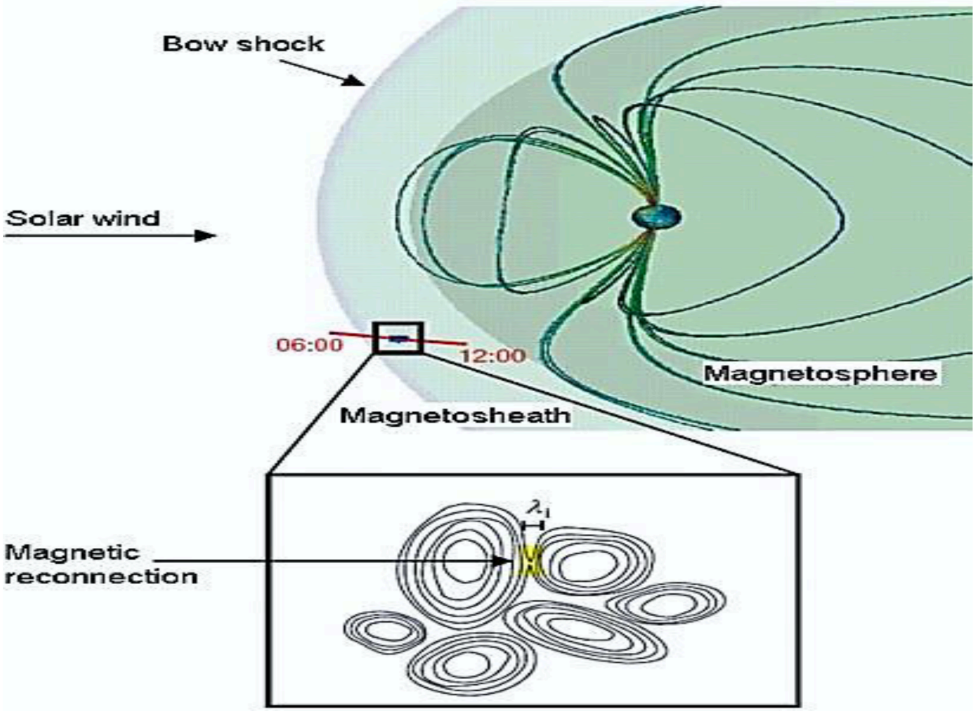

Figure 4: Schematic diagram of the magnetosheath transition region at 65000 km. Magnetic reconnection region are shown in rectangle below the main figure (courtesy to NASA/ESA)

.

layer needs to be measured within Earth dipole magnetic field average strength $|B|$.

2.3 Open magnetopause

The formation of the Earth magnetopause i.e. outermost open magnetic field line l_n boundary surface layer transition region is classified in this section. At equatorial plane the solar wind plasma particles induce the 1^{st} order perturbation into Earth magnetic dipole field. It leads to the Earth magnetic dipole field changes in equatorial plane towards sunward earth radial distance $10.05R_E$ compressive higher magnetic field region of the resistive variable Earth magnetopause (Fujimoto & Phan & Toth, 2015). IMF variation induces the 2^{nd} order of perturbation in Earth magnetopause and, therefore, magnetic tension force i.e. F_{mt}. As a result, magnetic field and ions plasma particles

pressure induce the high energetic shock wave. The rotating northward IMF line and opposite polarity Earth outermost magnetic field line l_n interaction support magnetic field energy diffusion in shock wave at transition region (Burch et al., 2016, Fujimoto & Phan & Toth, 2015, Russell , 2016). This shock wave deforms and outermost compress the magnetic field line l_n surface of the sunward side of Earth magnetopause.

2.4 Plasma-sheet region

Thin electron plasma current sheet forms due to open magnetic field line of the sunward side as shown in Figure 3. Earth magnetopause surface solar wind pressure P_{sw} stressed by inner magnetic field three dimensional cross sectional area $A_{x,y,z}$ and reduce inside expanded magnetotail volume (Fujimoto & Phan & Toth, 2015, Russell et. al., 1998a). In plasma current sheet the electron plasma particles temperature (T_{0e}) in shock rest frame at initial time t_0 differ in comparison to space craft each shock frame(Petrukovich, 2015). Each transitioning time the electron plasma particles perpendicular temperature $T_{e\perp}$, pressure $P_{e\perp}$, pressure tension P_{ten}, velocity v_{up} increases.

2.5 Neutral-sheet

Earth northward side magnetic field known as neutral-sheet on north-ward side of neutral point-in magnetotail transition region(Fujimoto & Phan & Toth, 2015). Tail ward side electron plasma particles and south-wards magnetic field on tail ward side magnetosphere region e-plasma particles velocities variation occurs in thin e-plasma current-sheet (Petrukovich, 2015). Magnetotail expansion occurs at the rates of 20-100 km/s. A thin e-plasma current sheet forms at anti sun-ward side in half thickness i.e. 5 km.

3 The structure of the Collisionless shocks

The spatial scales of the electromagnetic field in the CS region is important, because it's related to the various physical processes involved in the shock formation. The structure of the shock depends on non-linear processes increasing steepening of a non-linear electromagnetic wave and processes which are preventing it. In case of CS in the Earth magnetosphere such a processes could be viscosity, anomalous resistivity and particle reflection from the front of CS. Pressure pulse generated by the solar wind increase the wave steepening and as a result magnetic field pressure P_B increases. A plasma to magnetic field pressure difference induce shock potential difference. Electrons drifting through the electric field which is induced by shock wave. A discrete phase space electro magnetic (EMW) and electrostatic waves (ESW) propagates at angle between the normal to the magnetic field and shock ramp θ_{kB}. An electron charge particles flow field alter at discrete phase angle from Earth magnetic field. Plasma pressure P_{sw} pulse steepening in magnetic field pressure P_B difference induce shock potential barrier, kinetic energy transform into heat resistivity arise in Earth bow sub-shock region (Russell et. al., 2007). Sunward side 15.23 resistive Earth bow sub-shock structure has three sub-domain regions (Bale, 2005):

- Foot
- Ramp
- Overshoot region

The cross-field plasma current induce turbulence at Earth bow shock front reducing reflection rate of the gyrating ions fraction occur. But increasing bulk ions temperature behind shock transition, as a result, any new incoming ions reflection doubling averaging magnetic thickness and upstream directional electron plasma heat flux.

Ion plasma kinetic energy transforms into heat flux and induce ramp $\frac{\delta B}{B_0}$. In Earth bow shock wave the magnetic ramp width variation occurs at critical Mach number (Krasnoselskikh et al., 2013). The thickness of the bow shock is proportional to the gyrating down stream the ion plasma (Mozer & Sundkvist, 2013). The reflection of ions from magnetic field may induce small or large amplitude magnetic structures (Wilson, 2013). Variation of magnetic ramp region occurs due to changes of electron upstream directional gyro-radial flow planer polarisation and wave propagation direction.

3.0.1 QPS structure formation

In this work QPS structure was analysed at several different times between 2001 and 2015. IMF barrier control interaction rates of the electron, ions plasma particles with resistive northward magnetic curvature line boundary surface layer. Kinetic ion pressure ($P_{\|}$ and $P_{\perp}$) variation compress resistive Earth magnetic field. During this process ion kinetic energy transforms into thermal energy. As a result, magnetic field variation occurs in magnetic ramp transition region in QPS front within angle between shock normal and upstream magnetic field. Fraction of the ion kinetic energy and thermal energy dissipates and dispersion rates changes on QPS surface. Shock wave upstream surface interacted and less energetic electron plasma charge particles gain energy. Energetic electron plasma particles gyro radial motion variation induces in 3D velocities v_x, v_y, v_z space on B_x, B_y, B_z surface in ramp region of QPS front. Induced electric field E_x, E_y de-accelerates ions plasma particles in downstream and accelerates an electron plasma charge particles into upstream direction. Anticlockwise upstream electron plasma particles cross couples with magnetic field B_x, B_y, B_z in QPS front as shown in Figure 5. Wave-particle interaction in ramp region induces energy variation at each upstream magnetic field to wave propagation angle θ_{Bk}. QPS evolves from steepening plasma pressure ($P_{\|}$, $P_{e\perp}$), divided into number of small plasma amplitude steepening

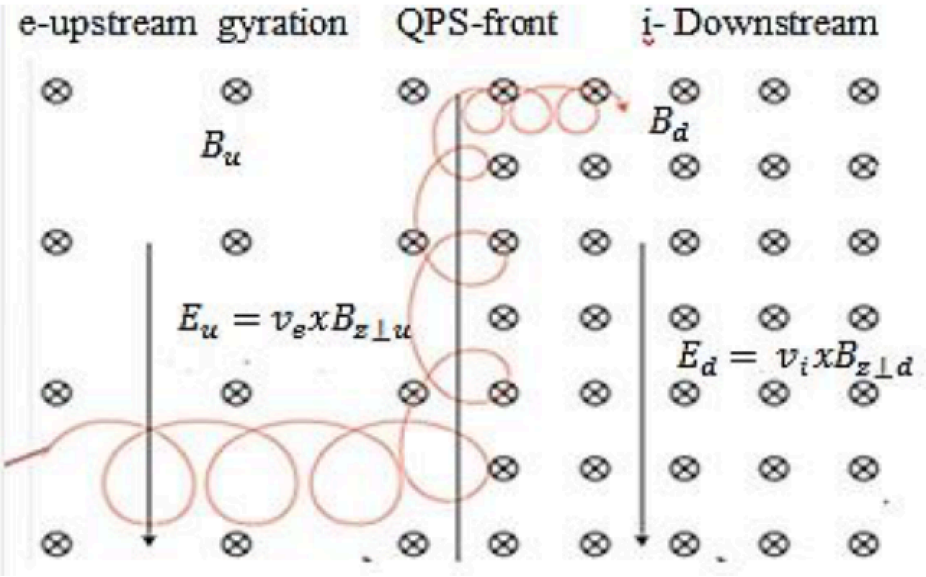

Figure 5: Schematic representation of physical motion of plasma particles at Quasi Perpendicular Shock (QPS)

waves in upstream ramp region.

Kinetic ion-electron plasma pressure $P_{\|}$, $P_{\perp}$ to magnetic pressure P_M variation is different at each resistive Earth magnetic field line at each angle between shock normal and upstream magnetic field θ_{Bn}. A down stream internal ions energy density flow to upstream electron internal energy density flow ratio is a function of the Mach number can be classified within each resistive each magnetic field boundary surface layer form ramp region. A discrete phase velocity v_{phe} relies on magnetic field perturbation in magnetic ramp. Ions density n_i increases on the resistive Earth magnetic field line boundary surface in ramp region. But de-accelerated ions density changes into downstream high magnetic field in QPS front magnetic ramp region at each angle between shock normal and upstream magnetic field. As a result, magnetic pressure P_M variation increases in resistive the Earth magnetopause magnetic field curvature line. An ion diffusion region variation occurs with magnetic strength at resistive each magnetic field curvature line boundary surface layer transition region.

3.1 Cluster satellites instrumentation used for CS identification

Cluster satellites C1-C4 have three different types of instruments used to detect magnetic field and plasma parameters, e.g.:

- Fluxgate Magnetometer (FGM). Four Fluxgate Magnetometers were used on board of Cluster satellites. They are able to measure elliptically polarised magnetic field variation rates within TDS mode in ramp region of QPS front. PPSNS autonomously guides FGM to detect variations of magnetic field at QPS front with a high time resolution, i.e. 5-vector per second. Shock normal magnetic field B_n and shock normal vector n_x, n_y, n_z are detectable using MVA numeric computational PPS measurement method. The shock normal magnetic field B_n detection methodology explained further in Chapter 4.

- Hot ions Analyser (HIA). The Hot Ion Analyser (HIA) instrument select upcoming ions accordingly to their energy by using electrostatic deflection in a symmetric quadro-spherical analysing system. This system has a uniform angle-energy response and fast particle imaging detection which is based on micro-channel plate electron multipliers and position encoding discrete anodes. The data received by this instrument and analysing method discussed in Chapter 4, Subsection **??**.

- Cluster Ions Spectroscopic (CIS). Cluster Ions Spectroscopic (CIS) instrument is highly sensitive to detect thermalised reflective in downstream high magnetic field ions. An upstream B_x, B_y, B_z surface cross coupled with gyrating electron plasma particles with energies 0.1 up to 10 KeV (Russell et. al., 1998a, Sizov, 2010, Yamakawa, 2014).

Precise Positioning Satellite Navigation System (PPSNS) autonomously guides these instruments which are capable to detect CS, Earth bow shock and QPS structure formation in a real time (Balikhin et al., 2002, Bale, 2005, Russell , 2016).

3.2 Quasi Perpendicular Shock region segmentation

Three different precise positioning segmentation processes can be classified as:

- Earth bow shock at $15.23R_E$ and sunward $10.5R_E$ magnetopause magnetic field region QPS structure space domain region segmentation;
- Cluster PPSNS at elliptical inclination trajectory path autonomously control shock structure formation space domain region segmentation;
- QPS inertial motion frame rates sampled real time PPS magnetic field and plasma variable data transform into the user mode segmentation.

At sunward side radial distance $15.23R_E$ Earth bow shock potential thick barrier form 200 km to 300 km variation region at 90000 km attitude de-accelerated supersonic solar wind plasma decouples from IMF (Balikhin et al., 2002, Balikhin, 2014, Bale, 2005, Fujimoto & Phan & Toth, 2015, Russell et. al., 1998a). Earth bow shock surface ions and electrons plasma particles thermalised and energises rates changes with angle between shock normal and upstream magnetic field θ_{Bn}.

An energetic ions, electron plasma particles accelerated towards $10.02R_E$ megnetosheath to sunward side $10.05R_E$ resistive Earth magnetopause region. 2^{nd} order perturbation at sunward side $10.05R_E$ resistive Earth magnetopause transition region compress magnetic field line boundary surface layer form resistive QPS wave in ramp front disperse into Earth magnetic field (Balikhin, 2014, Bale, 2005, Wilson, 2016). Real time precise positioning Earth bow shock and Quasi Perpendicular Shock (QPS) structure formation region segmented by PPSNS autonomously guided on board FGM, HIA, CIS instruments. Lambeth method used for Cluster PPSNS trajectory path correction at sunward $15.23R_E$ Earth bow shock to $10.05R_E$ magnetopause resistive magnetic field surface form QPS structure region.

3.2.1 Quasi Perpendicular Shock analysis methods

Three different methods were applied for identification of QPS structure formation in $10.04R_E$ Earth magnetosphere transition region:

- MVA - real time precise measurement method to analyse three component of magnetic field and magnetic ramp, wave propagation direction, shock normal, shock normal magnetic field;
- HIA - three dimensional velocities measurement and electron plasma parameters Precise Positioning System (PPS) real time numeric computation measurement method;
- Cluster Ions Spectroscopic (CIS) - three dimensional real time ions, electron plasma particles power spectral energy density variation measurement method.

3.2.2 Spacecraft axial gyro motion variation classification

Cluster constellation has Precise Positioning Satellite Navigation System which is autonomously guided Fluxgate Magnetometer (FGM), Cluster Ion Spectroscopic (CIS), Hot Ion Analyser(HIA) instruments to detect transition region of the CS. Pre-Shock wave velocity transition occurs in the Earth magnetic dipole field (in horizontal direction of initially unpolarised magnetic field B_0). GSE plasma shock rest frame schematic diagram is shown in Figure 6. Y_{GSE}, R_E spacecraft 3D frame considered as moving on sunward side of perturbed Earth magnetopause. CS wave dispersion relation normalised into X_{GSE}, R_E plasma shock rest frame corresponds to the direction of propagating k-waves at upstream directional angle to magnetic field θ_{Bk} velocity variation with time detected in satellite separation vector R_1, R_2, R_3 at elliptically polarised arc length scale s_{12} and s_{14} in TDS mode (Balikhin, 2014, Burch et al., 2016, Wilson, 2013). The electron plasma particles flow used to measure the resistive shock wave velocity $\simeq$ ratio

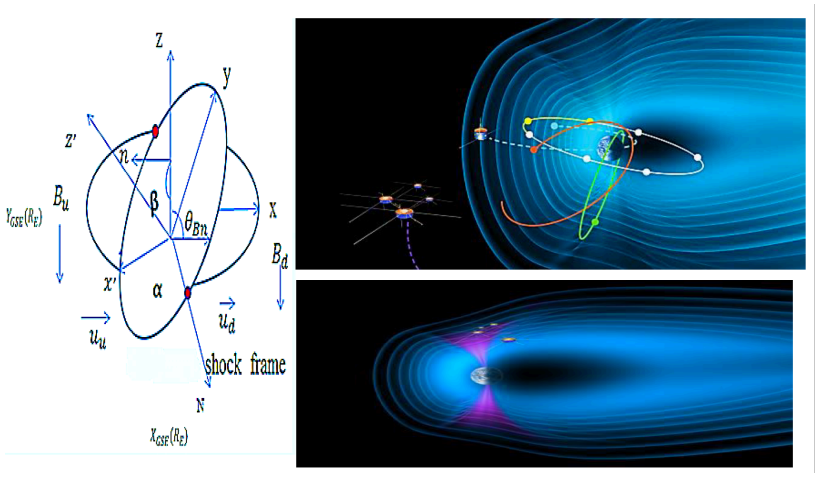

Figure 6: The trajectory orbits of satellites: (i) Cluster spacecraft C1-C4 as shown in purple; (ii) ESA Double Star TC-1 cluster satellite (blue) trajectory; (iii) 64000 km altitude earth Magnetopause-to-Aurora Global Exploration (IMAGE) cluster satellite (green); (iv) GOES cluster satellite (yellow); (v) Five geosynchronous orbital inclination path of the satellites (courtesy to ESA).

of the satellite separation distance $\pm$ to short time duration in TDS. The Earth magnetosphere magnetic field variation changes between 0.1 - 0.6 Gauss due to influence of solar wind thermal pressure P_{sw} (Fujimoto & Phan & Toth, 2015, Russell et. al., 1998a).

3.2.3 QPS transition time classification

Each Earth magnetic dipole field perturbations occur in horizontal direction in equatorial plane toward high magnetic field region of the Earth magnetopause. As a result, outermost compress magnetic field curvature surface solar wind to magnetic field pressure variation induce 2^{nd} order perturbation on sunward side of Earth magnetopause surface. Back and forward pressure non-linear oscillation induces wave modes in QPS front magnetic ramp region and emits energy. Excited propagating waves carry e-plasma particles

mass m_e momentum and energy from 2^{nd} order perturbation at sunward side $10.05R_E$ of magnetopause resistive magnetic ramp to magnetosheath transition region drifting toward northward side region. Transitioning e-plasma particles mass momentum and energy is conserved (Balikhin, 2014, Bale, 2005, Fujimoto & Phan & Toth, 2015). Some fraction of ions kinetic energy transforms into heat ($T_{\parallel}$, $T_{e\perp}$) which is dissipate in 3D shock inertial region. QPS energy transition changes electron plasma and magnetic field parameters, i.e. Earth magnetopause surface induce shock potential barrier and compress magnetic field line surface.

In QPS front ions-ions instability induces transverse intermediate wave mode known as Alfvén wave. Inductive electric field de-accelerates ion particles in down and induces slow ion whistler wave mode. Inductive electric field E_x, E_y accelerates electron plasma particles into upstream directional space domain region and induce fast wave propagation mode (Balikhin, 2014, Bale, 2005, Wilson, 2016). Ions phase (positive and negative) space and B-field upstream phase variation at the magnetic ramp $\frac{\delta B}{B_0} \simeq 5.1nT$ egion is shown at Figure 7 at shock transition time 2014-04-20 T11:23:20UT.

As an example, QPS and magnetic variation on 2014-04-30 T12:18:00UT are shown in Figure 8. Magnetic filed magnitude changes from B_{min} $\simeq$10nT at foot region up to maximum value $B_{max} \simeq$ 40nT in magnetic ramp region. 2^{nd} order perturbation into Earth magnetopause resistive magnetic field diffuses due to heavy thermalised ions multiple times interaction at magnetopause surface. Partially diffused magnetic energy plasma particle transforms into thermal $T_{\parallel}$, $T_{\perp}$ and ions kinetic energy dissipates on shock wave surface. This observation of the QPS is important for understanding of the physical plasma processes (for example energy redistribution in the QPS front) and comparison with existing theoretical Paredu models (will be shown below).

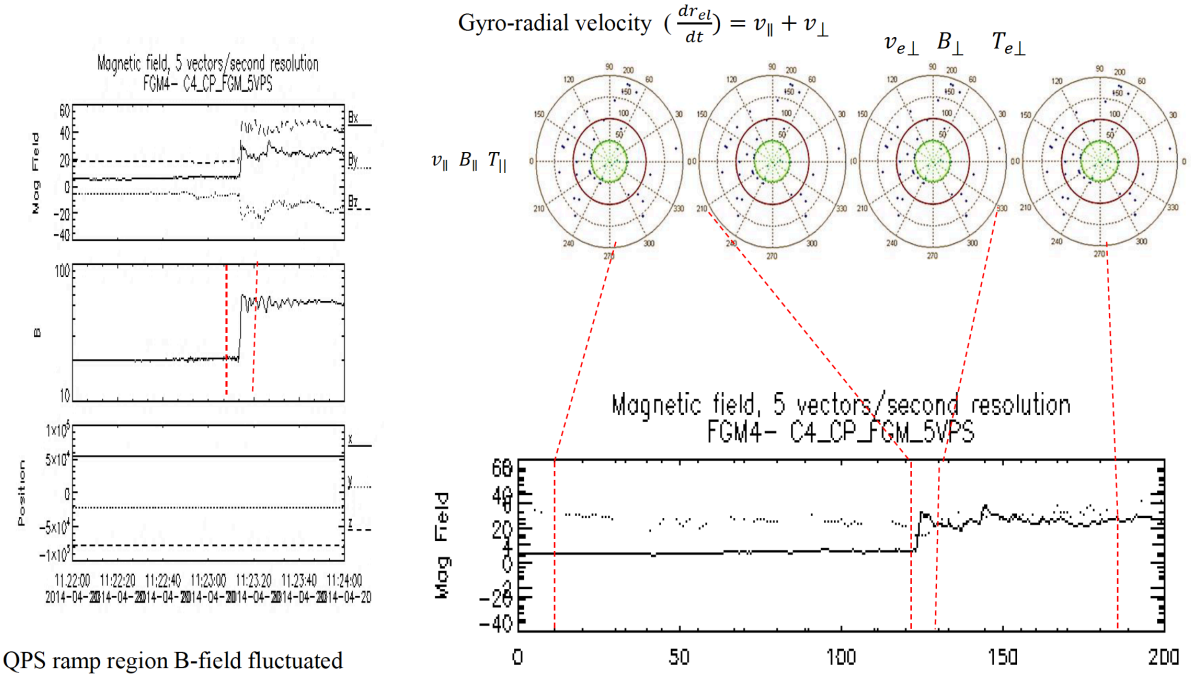

QPS ramp region B-field fluctuated as shown figure panel-2

Figure 7: Fluctuation of magnetic field at QPS front magnetic ramp region are shown at the left panel. QPS transition at 2014-04-20 T11:23:20UT are shown at the right panel. An ion phase variation distribution in QPS front are shown on top of the figure.

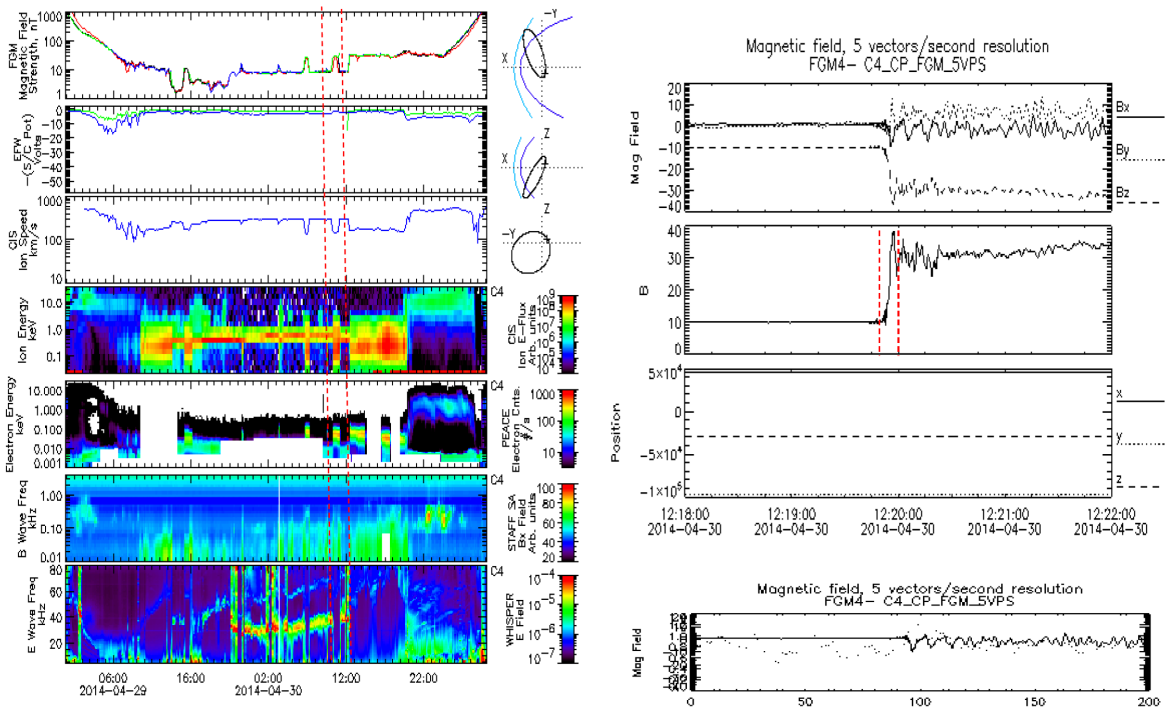

Figure 8: QPS detected on 2014.04.30 T12:18:00UT. The region of magnetic variation at QPS front are shown in vertical red colour doted line (left panel).

3.3 Computation of the Earth Magnetic Ramp

The analysis of magnetic field variation at the ramp of QPS as a function of Mach number (M) and perturbation of magnetic ramp as a function of the angle variation between shock normal and upstream magnetic field are remaining gap in studies of the QPS. These dependancies will lead to the possibility to analyse (and what is more important to obtain) the electron plasma parameters in the bow shocks around the perturbed Earth magnetopause and other planets. This is not a simple task because this statistical numeric computation data operation and analysis work is limited by the number of such an events.This is require analysis of as many as possible QPS crossing events measured by C1-C4 Cluster satellites during it's mission (2001-2015).

The difference between minimum magnetic field magnitude B_{min} in shock front foot region and maximum magnetic field magnitude B_{max} at the magnetic ramp transition region can be calculated as as:

$$\frac{\delta B}{\bar{B_0}} \simeq \frac{B_{max} - B_{min}}{\bar{B_0}}$$

The Earth magnetic ramp $\frac{\delta B}{\bar{B_0}} \simeq 4.76$ nT in QPS front measured at 2^{nd} order perturbation in resistive Earth magnetopause magnetic field on 2014-04-30 T12:18:00UT are shown Figure 8. The results of identification of QPS on 2014.12.05 at 03:05:00UT are shown in Figure 9. Upstream magnetic field to shock normal angle $\theta_{Bn} \simeq 59.39$, shock normal vector ($n_x \simeq 0.6132$, $n_y \simeq 0.5757$, $n_z \simeq -0.5408$) are shown in the same figure. Thermalised electron density $n_i \simeq 23.5cm^{-3}$ in ramp transition region of QPS front detected by CIS HIA are also shown.

Reflective thermalised ion cyclotron clockwise gyro radial velocity v_i variation in down stream high magnetic field ramp region in QPS front was detected by HIA sensor as shown left-hand side of Figure 9 at 16-02-2015 T11:08:00UT. Thermalised kinetic

ion energy $\simeq 0.05KeV$ at $10.05R_E$ was detected at 16-02-2015 T11:08:00UT. Incoming ion kinetic energy transforms into thermal and doubling magnetic thickness into downstream region. Partially diffuse magnetic energy transforms kinetic energy of ions into thermal energy and dissipates on QPS upstream surface. As a result, discrete ions power spectral energy density changes at downstream resistive surface.

Numerically were analysed the following shock transition events:

- shock crossing by the Cluster C3 spacecraft on 19.02.2002; 19.03.2001; 31.03.2001; 19.02.2002; 19.02.2003; 15.01.2004; 10.01.2004; 14.01.2012; 10.01.2013; 10.02.2013; 10.09.2013; 15.02.2014; 03.06.2014; 16.02.2015. For example, see Figure 8 where three components of magnetic field measured by Cluster C1-C4 during crossing the terrestrial Earth bow shock on 30-04-2014T12:18:00 are shown;

- Three components of magnetic field B_x, B_y, B_z at the ramp region shock front detected as shown in right hand side of Figure 8 on 2014-04-30 T12:18:00UT.

- Ramp $\frac{\delta B}{B_0} \simeq 4.75nT$ measured at QPS crossing time as shown in Figure 8 on 2014.04.30T12:18:00UT;

- Magnetic field B_x, B_y, B_z in ramp $\frac{\delta B}{B_0}$ detected during the QPS crossing time on 2014.03.13 at 02:15:00UT. Shock wave magnetic field measurements on 2014.01.07;

- Shock wave magnetic field measurement at QPS crossing on 2013-05-16T 03:52:00UT;

- Ramp $\frac{\delta B}{B_0}$ detected during the QPS crossing on 2014-03-30T10:22:00UT.

- Shock normal magnetic field B_n components B_x, B_y, B_z variation at the ramp with angle between shock normal and upstream θ_{Bn} measurement by MVA method.

3.4 Summary

In this chapter we provided the following points:

- detection and analysis of CS, Earth bow shock and QPS structure formation within Earth magnetosphere subdomain region;
- based on in-situ measurements of the 1^{st} and 2^{nd} order perturbation in the Earth magnetopause resistive magnetic field, the computed values of the Earth magnetic field ramp $\frac{\delta B}{B_0}$ gives an opportunity to identify the Mach numbers and as a result, plasma parameters;
- calculation of magnetic ramp within angle between shock normal and upstream magnetic field between 2001- 2015 are shown in Table 1.

4 Detection of QPS normal and wave propagation

QPS wave energises electron plasma particles and, therefore, gyro-radial velocity v_{up} increases in upstream direction. At the same time, thermalised ions reflected back into downstream at 2^{nd} order perturbation and compress Earth magnetopause resistive magnetic field (Balikhin, 2014, Fujimoto & Phan & Toth, 2015, Wilson, 2013).

Diffused magnetic energy transforms kinetic energy of ions into thermal which dissipates on QPS wave surface. Elliptically polarised magnetic field B_x, B_y, B_z at QPS ramp induces gyro-radial $r_{el} \simeq \frac{v_{up}}{\omega_{pe}}$ distance variation of electron plasma particles. Electron plasma particles motion changes within elliptically polarised magnetic field B_x, B_y, B_z at ramp $\frac{\delta B}{B_0}$ transition region within angle between shock normal and upstream magnetic field in range $45 \leq \theta_{Bk} \leq 90$.

4.1 Shock normal and direction of wave propagation calculations. MVA method

The magnetic field B_x, B_y, B_z variation in ramp transition region of QPS within angle between shock normal and upstream magnetic field θ_{Bn} detected by MVA computation method.

The measurements of magnetic field variation is averaged on N point positioning real time numeric computation within satellite separation vector R_1, R_2, R_3 at elliptically polarised arc length scale s_1, s_2, s_3 in finite forward time series scale step t_n. The three components of magnetic field averaged as follows:

$$\bar{B_x} = \frac{1}{N} \Sigma_{i=1}^{N} B_x^i$$

$$\bar{B_y} = \frac{1}{N} \Sigma_{i=1}^{N} B_y^i$$

$$\bar{B_z} = \frac{1}{N}\Sigma_{i=1}^{N} B_z^i$$

Average measured value of the magnetic field components are $B_x \simeq 3.58$nT, $B_y \simeq 6.16$nT and $B_z \simeq 5.03$nT and shown in Figure 9 at time 16-02-2015 T11:08:00UT. Magnetic strength $|B|$ measurements are shown in Figure 11 at 2014-1-11 T22:51:00UT. Fluctuated magnetic field within magnetic ramp transition region at QPS wave transition time initially rising magnetic field magnitude from minimum magnetic field B_{min} in shock front foot region up to maximum magnetic field $B_{max} \simeq 45.9nT$ in magnetic ramp $\frac{\delta B}{\bar{B_0}} \simeq 3.9nT$ in QPS front numerically measured using MVA PPS and shown in Figure 9 at 16-02-2015 T11:08:00UT. Inhomogeneous horizontal directional magnetic field variation average $B_0 \simeq 9.32nT$ value measured using point spread TDS mode detection method. Shock front induces a foot transition region as shown in Figure 9 at 16-02-2015 T11:08:00UT. Ions scattering angle between shock normal and upstream magnetic field θ_{Bn} changes at each phase space. The ion density n_i pressure induces 2^{nd} order perturbation at $10.05R_E$ resistive Earth magnetopause magnetic field. The increase of kinetic ion plasma particles density n_i compress magnetopause and induces the different size of restive magnetic field vertices at high magnetic field Reynolds number $100 \leq R_M \leq 200$.

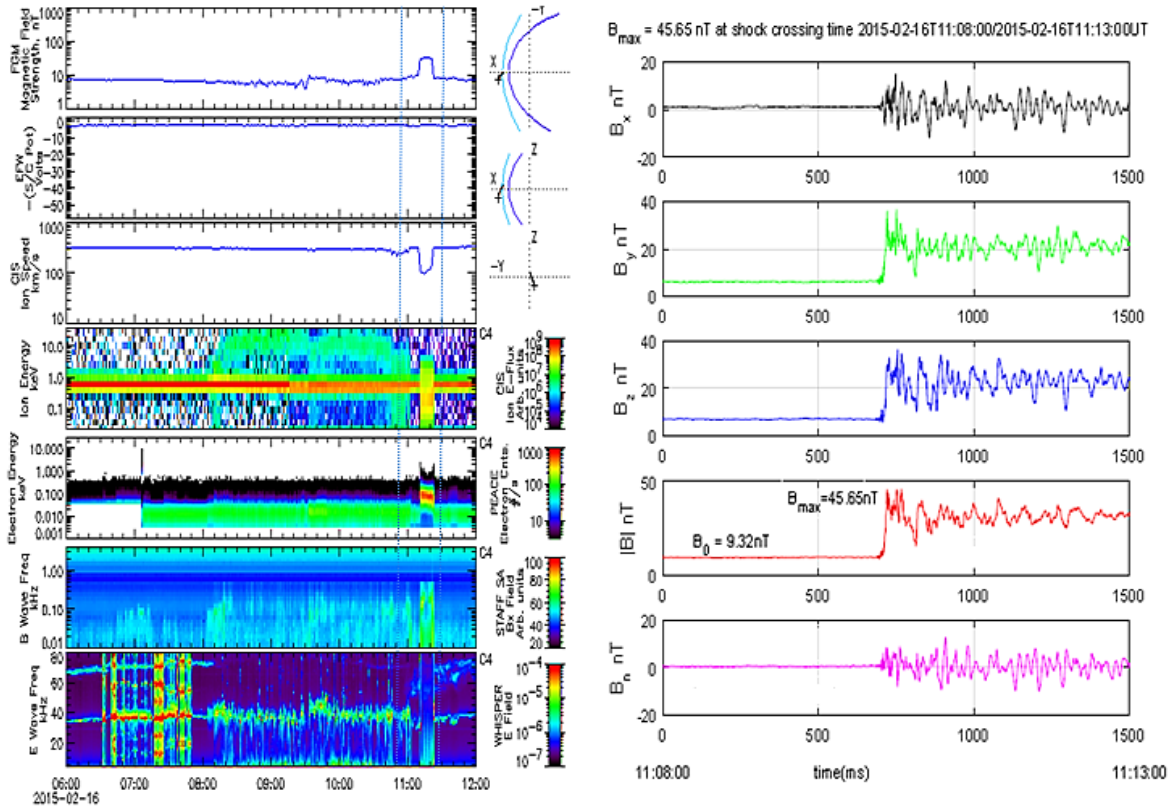

Figure 9: The measurement of the magnetic field (FGM), ion density, ion velocity, ion energy, and electron energy are shown on the left side of the image from top to bottom correspondingly. Initially unpolarised magnetic field measured at level $B_0 \simeq 3.9nT$ at the front of QPS at 16-02-2015 T11:08:00UT.

4.1.1 Shock normal measurements

Upstream magnetic field B_{up} and downstream of QPS are stationary within 0^{th} order GSE plasma shock at initial arc length scale s_0 and at initial time step t_0. 1^{st} order up to n^{th} order GSE spacecraft shock frame is moving across perturbed resistive the Earth magnetopause resistive magnetic field line boundary curvature surface layer. Magnetic field variation at transition region measures shock normal vector n_x, n_y, n_z within satellite separation vector R_1, R_2, R_3 in elliptically polarised arc length scale s_1, s_2, s_3 in finite time series t_n. Real time shock normal vector (n) can be calculated as:

$$n = \pm \frac{(B_d \times B_{up}) \times (B_d - B_{up})}{(|B_d \times B_{up}|) \times (|B_d - B_{up}|)}$$

A minimum variance of the shock normal vector n_x, n_y, n_z of the elliptically polarised magnetic field at QPS crossing in finite forward time series scale step t_n normalised into equation

$$\varsigma = \frac{1}{N} \Sigma_{i=1}^{N} (B^i \cdot n - \bar{B} \cdot n)$$

Here N is the number of magnetic field point measurements, B^i represent 1^{th} up to N points of measurements of the elliptically polarised magnetic field B_x, B_y, B_z within angle between shock normal and upstream magnetic field. In particular, $B_x \simeq 3.59$ nT, $B_y \simeq 6.16$ nT and $B_z \simeq 5.03$ nT for the shock normal $n_x \simeq 0.6132$, $n_y \simeq 0.5757$, $n_z \simeq -0.5408$ at time 16-02-2015 at time11:08:00UT as shown in Figure 9.

4.2 Shock normal measurement (PPS method)

Elliptically polarised magnetic field B_x, B_y, B_z components average value and shock normal n_x, n_y, n_z variation measured by using MVA method within satellite separation vector R_1, R_2, R_3 at elliptically arc length scale s_1, s_2, s_3 in finite forward time series

scale steps. The normal magnetic field B_n can be calculated as:

$$B_n = \bar{B}_x n_x + \bar{B}_y n_y + \bar{B}_z n_z$$

Shock normal variation $B_n \simeq 3.03nT$ at QPS transition time are shown in the RHS of Figure 9 for date/time 16-02-2016 T11:08:00UT. Field aligned ion beam variation in ramp $\frac{\delta B}{B_0} \simeq 3.9nT$ region changes shock normal magnetic field value $B_n \simeq 3.03nT$ also shown on the same figure. The shock normal magnetic field average value B_n was also measured at several others times during 2001-2015.

4.3 Computation of the angle between shock normal and upstream magnetic field

IMF line barrier controls ion, electron plasma particles interaction with variable Earth magnetic dipole field distance B_{DC} at equatorial plane B_0 surface at sunward side at $10.02R_E$. The angle between shock normal and upstream magnetic field θ_{Bn} variation occurs in shock front transition region. Magnetic strength $|B|$ at the ramp front at QPS can be calculated as

$$|B| = \sqrt{\bar{B_x}^2 + \bar{B_y}^2 + \bar{B_z}^2}.$$

Upstream and downstream magnetic field B_{up} and B_d variations depends on angle variation θ_{Bn} between shock normal and magnetic field across QPS wave. QPS wave upstream surface thermalised e-plasma particles density n_e perturbation on elliptically polarised B_x, B_z, B_z surface induce e-plasma particle gyro radial motion variation with angle between shock normal and upstream magnetic field θ_{Bn}. Angle variation between

shock normal and upstream magnetic field θ_{Bn} at ramp region of QPS front is:

$$\theta_{Bn} = \tan|\frac{B_t}{B_n}|$$

$$\theta_{Bn} = \tan|\frac{(n \times B) \times n}{B.n}|$$

Ions thermal pressure changes magnetic strength $|B|$ at each angle between shock normal and magnetic field θ_{Bn} in ramp transition region at QPS front were calculated for the period between 2001-2015. Magnetic strength variation with angle between shock normal and and upstream magnetic field θ_{NBn} are shown in Figure 10.The lower magnetic strength is $|B| \simeq 1.8$ nT at $\theta_{Bn} \simeq 44.6$ detected at 2008-08-04 T03:57:00UT. As a result, magnetic strength $|B|$ variation in QPS front ramp region is indirectly changes e-plasma particles 3D motion.

4.4 Methodology used to measure the Alfvén velocity

The value of Alfvén velocity at QPS surface depends on fluctuated elliptically polarised magnetic field component B_x, B_y, B_z and electron plasma density n_e, e.g.

$$v_A = 19.2\sqrt{\frac{\bar{B_x}^2 + \bar{B_y}^2 + \bar{B_z}^2}{4\pi\bar{n_e}}}.$$

Magnetic strength ($|B|$) compress Earth magnetic dipole field at the non equilibrium point which is moving in horizontal direction at equatorial plane of the down gradient of the sun-ward $10.05R_E$ Earth magnetopause transitional magnetosphere and induces Alfvén velocity (v_A) (Balikhin, 2014, Burton, 1970, Kozlov, 2006). Elliptically polarised magnetic field average value $B_x \simeq 5.58$ nT, $B_y \simeq 6.16$ nT, $B_z \simeq 5.03$ nT at the ramp front gives magnetic strength $|B|$ measurement.

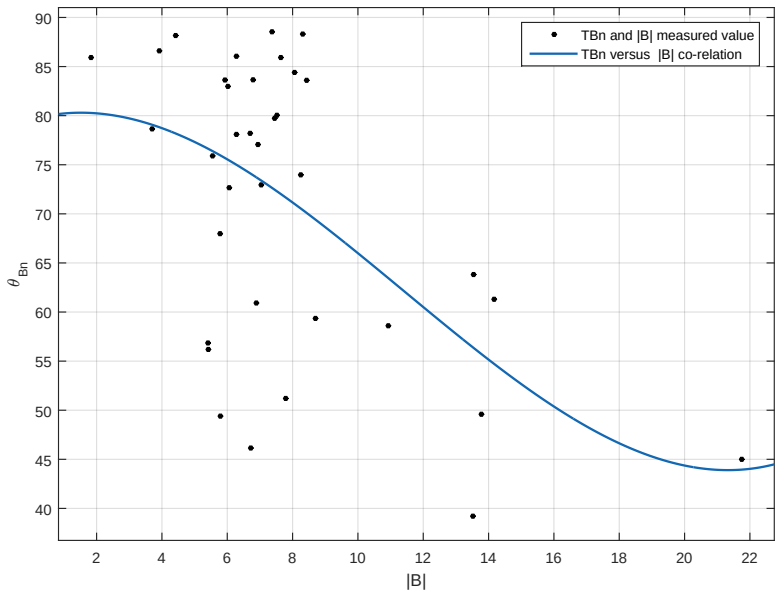

Figure 10: Angle variation within finite range $45 \leq \theta_{Bn} \leq 90$ between shock normal and upstream magnetic field as a function of magnetic strength $|B|$.

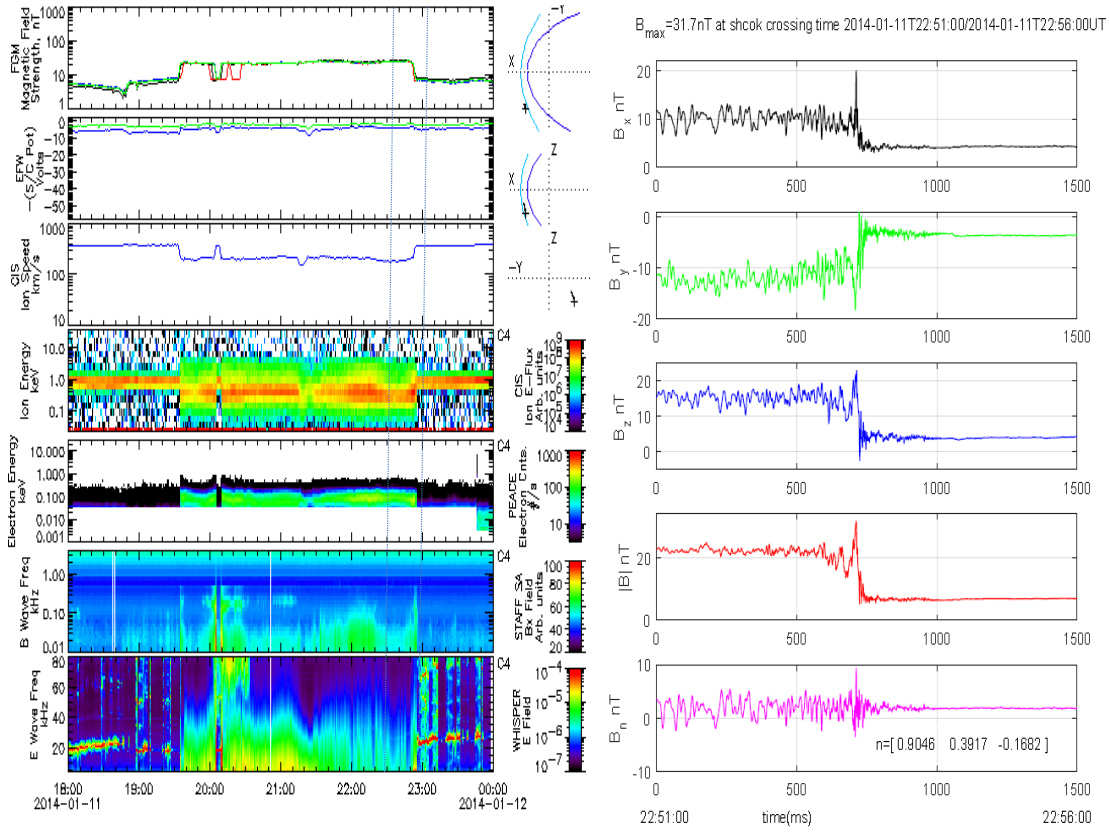

Figure 11: The measurement of the magnetic field (FGM), ion density, ion velocity, ion energy, and electron energy, B-wave frequency, E-wave frequency are shown on the left side of the image from top to bottom correspondingly.

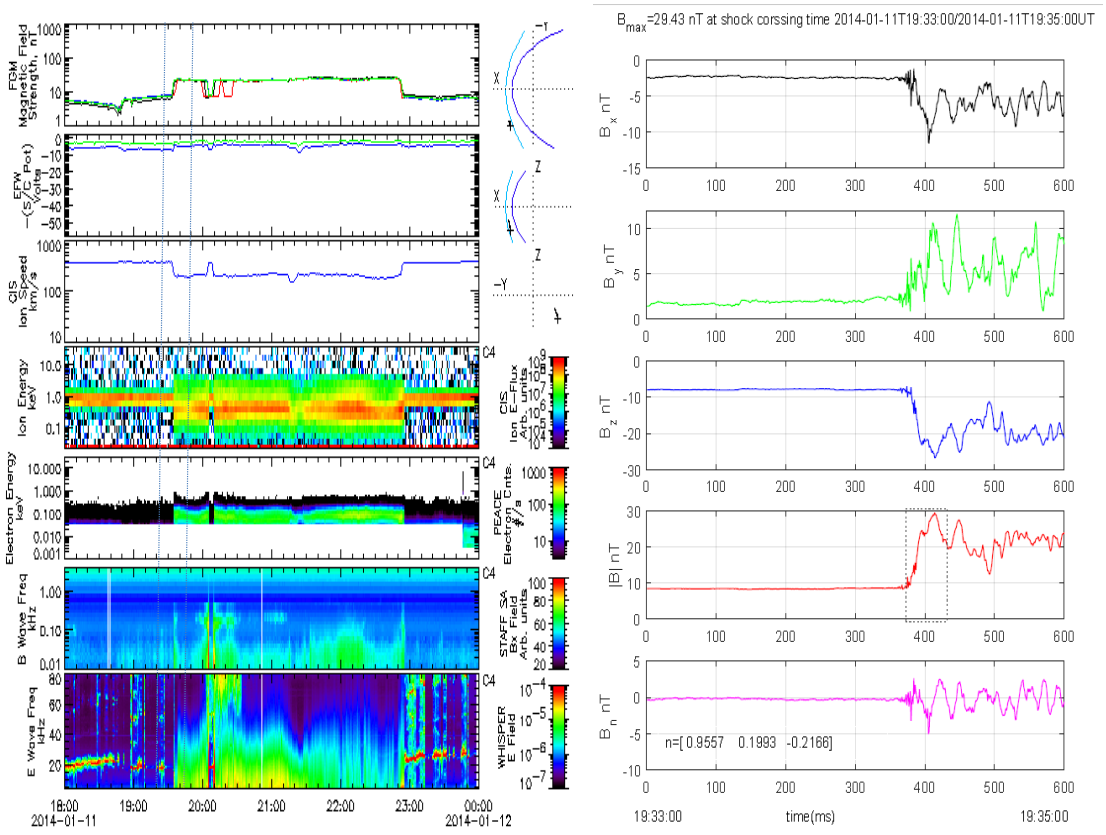

Figure 12: The measurement of the magnetic field (FGM), ion density, ion velocity, ion energy, and electron energy, B-wave frequency, E-wave frequency are shown on the left side of the image from top to bottom correspondingly. These values corresponds to the measurement on 2014-11-01 T19:33:00 - 2014-11-01 T19:35:00UT.

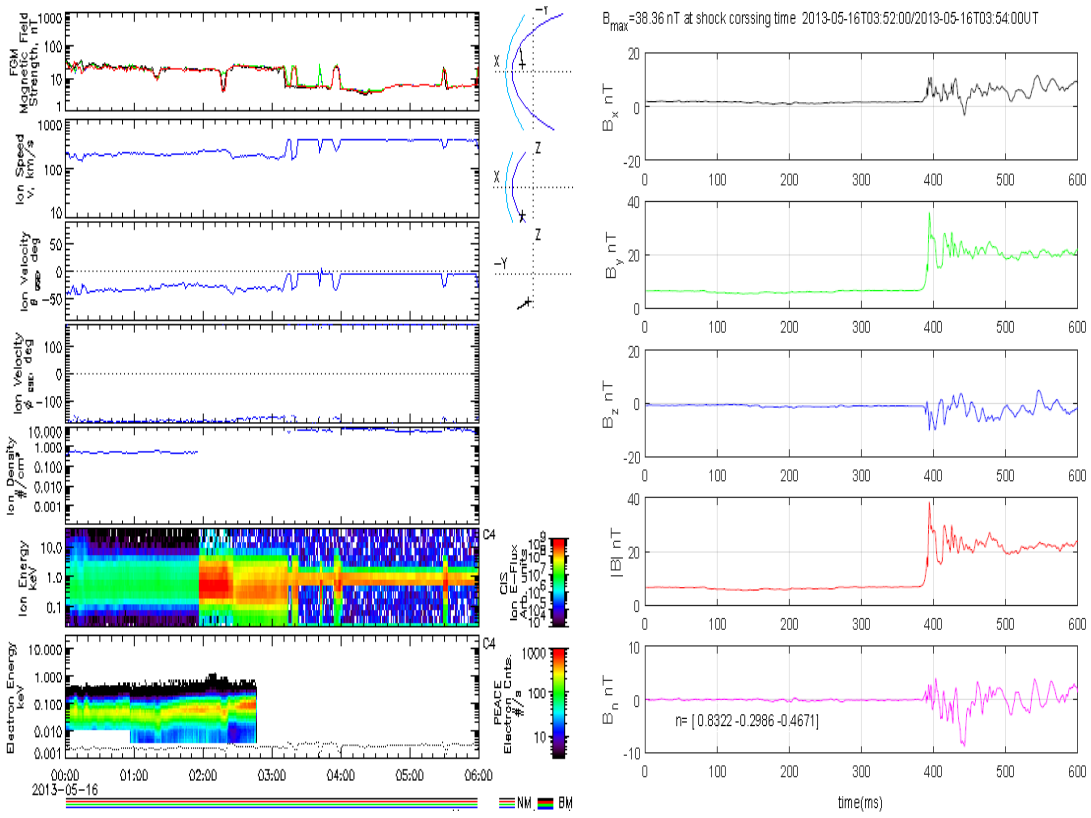

Figure 13: The magnetic field measurements (FGM), ion density, ion velocity, ion density, ion energy and electron energy $\simeq 17.4KeV$, at pressure tenser $P_{ten} \simeq 4nPn$ are shown on the left side of the image from top to bottom correspondingly. Shock normal magnetic field $B_n \simeq 1.02$nT value is shown on the right hand side and corresponds to the measurement on 2013-05-16 T03:52:00 - 2013-05-16 T03:54:00UT. Shock normal magnetic field $B_n \simeq 1.02$nT is increasing due to e-shock current density increase in ramp region within time 2013-05-16 T03:52:00 - 2013-05-16 T03:54:00UT

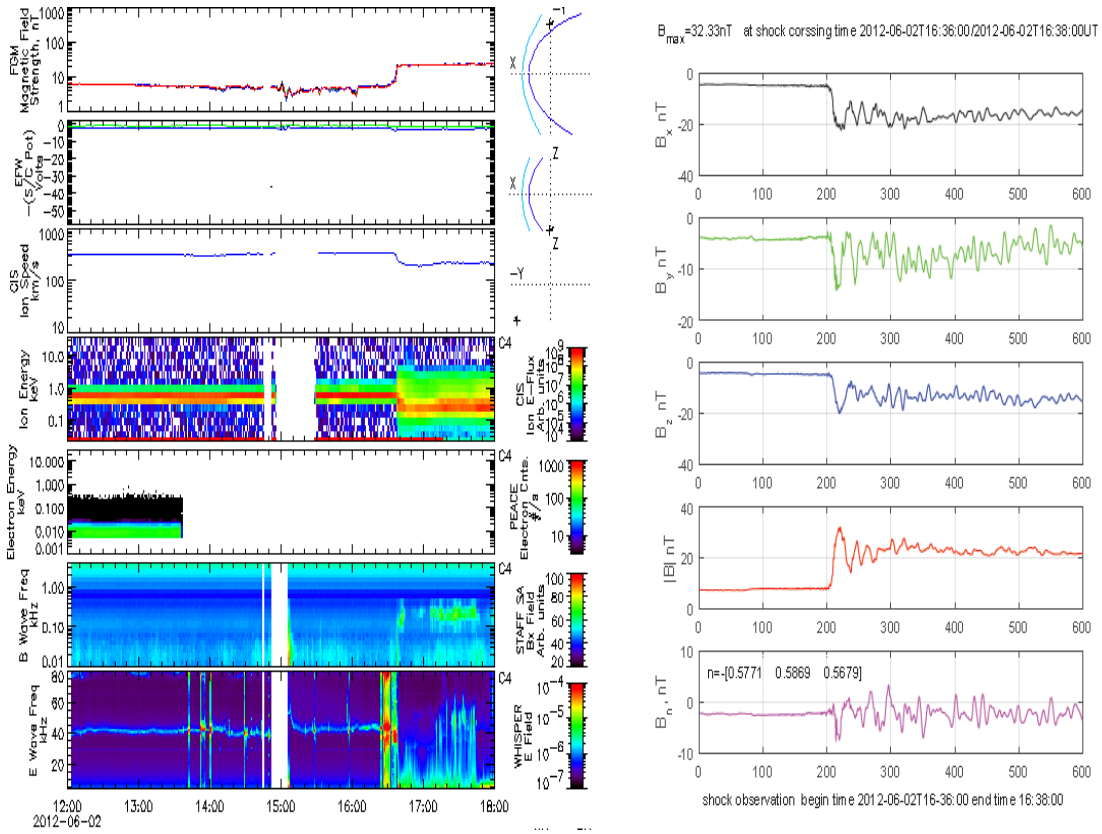

Figure 14: The measurement of the magnetic field (FGM), ion density, ion velocity, ion energy, and electron energy, B-wave frequency, E-wave frequency are shown on the left side of the image from top to bottom correspondingly. These values corresponds to the measurement between 2012-06-02 T16:36:00 - 2012-06-02 T16:38:00UT.

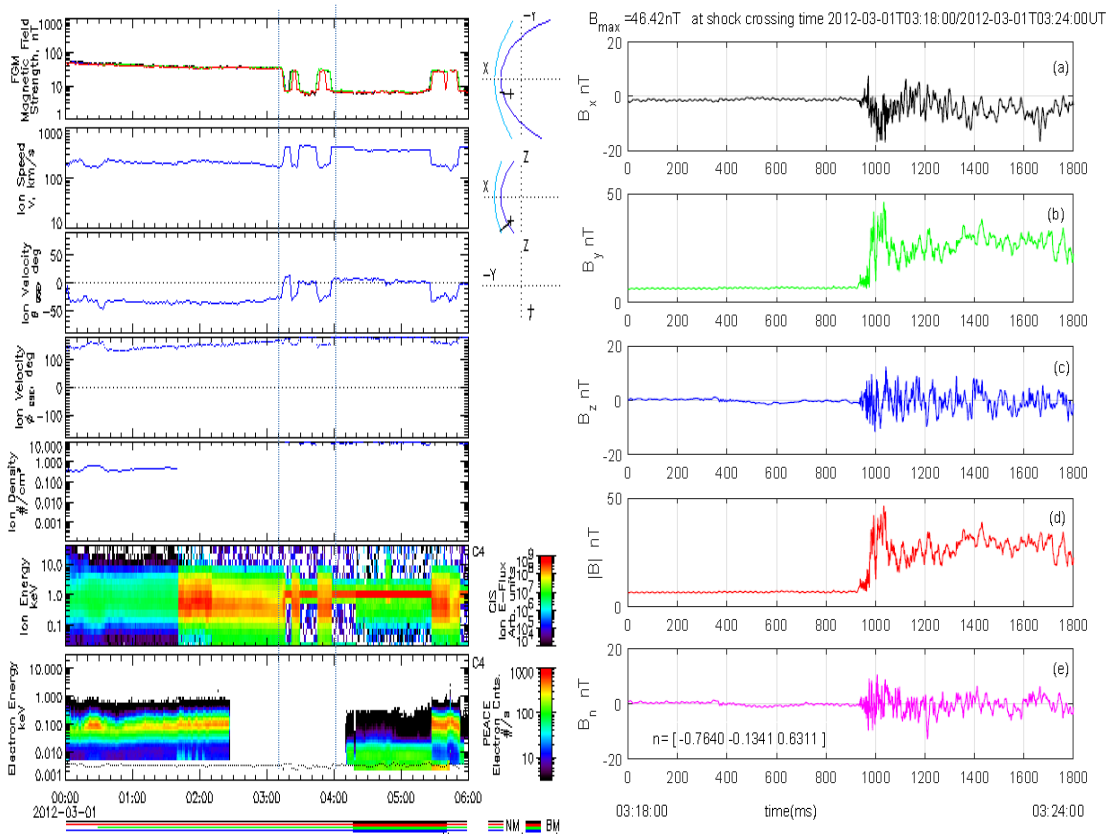

Figure 15: The measurement of the magnetic field (FGM), ion density, ion velocity, ion energy, and electron energy, B-wave frequency, E-wave frequency are shown on the left side of the image from top to bottom correspondingly. Magnetic field components measured by MVA PPS method. These values corresponds to the measurements between 2012-03-01 T03:18:00 - 2012-03-01 T03:24:00UT.

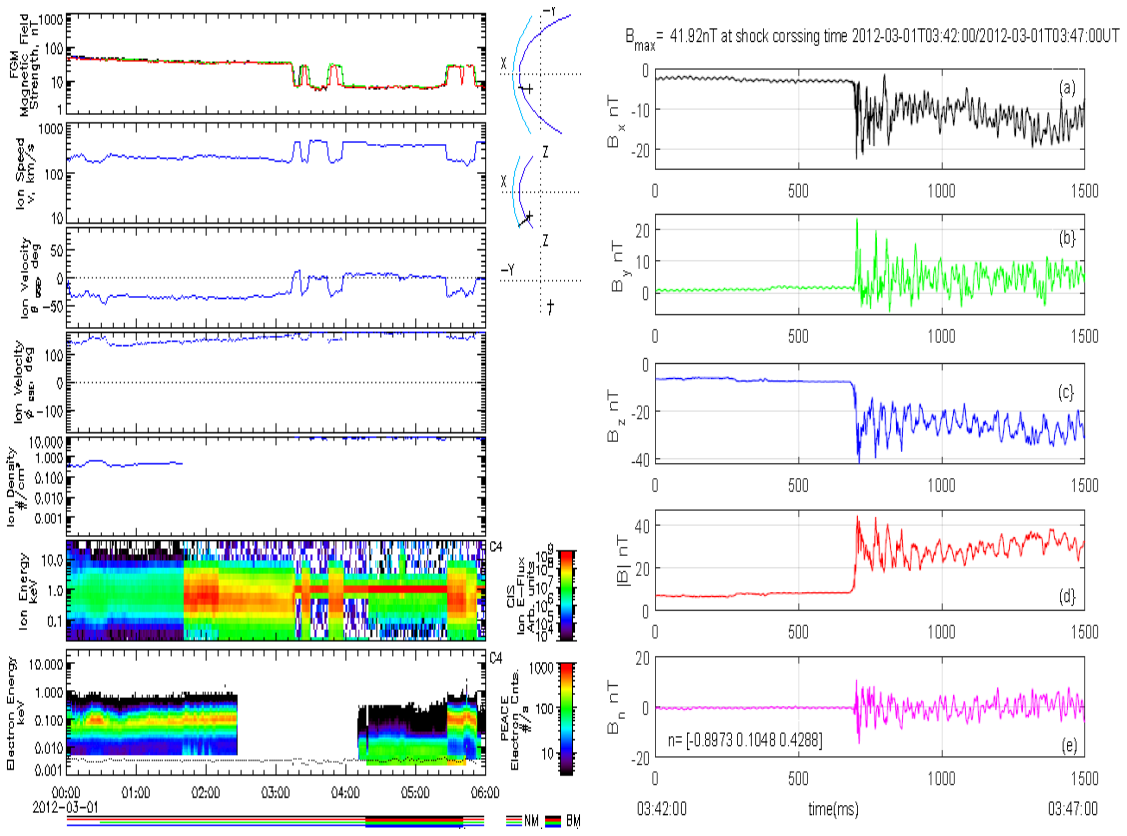

Figure 16: The measurement of the magnetic field (FGM), ion density, ion velocity, ion energy, and electron energy, B-wave frequency, E-wave frequency are shown on the left side of the image from top to bottom correspondingly. The Elliptically magnetic field magnetic field three components are $B_x \simeq 2.74$ nT, $B_y \simeq 1.74$ nT, $B_z \simeq 7.38$ nT as shown in right hand side panels. These values corresponds to the measurements between 2012-03-01 T03:42:00UT - 2012-03-01 T03:47:00UT.

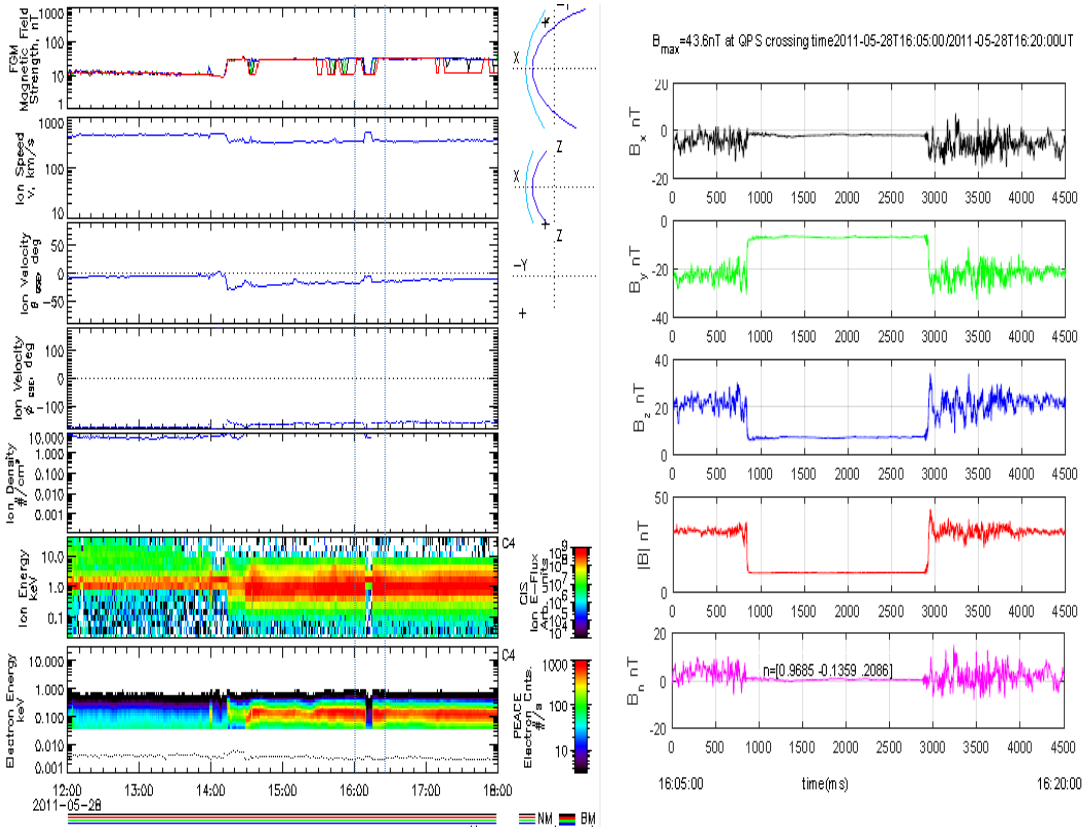

Figure 17: The measurement of the magnetic field (FGM), ion density, ion velocity, ion energy, and electron energy, B-wave frequency, E-wave frequency are shown on the left side of the image from top to bottom correspondingly. These values corresponds to the measurement on 2011-05-28 T16:05:00 - 2011-05-28 T16:20:00UT. Shock normal magnetic field $B_n \simeq 0.89$nT as shown in right hand side. Shock normal magnetic field $B_n \simeq 0.89$ nT rises due to e-shock current density increasing in ramp region at QPS transition time as shown at the middle.

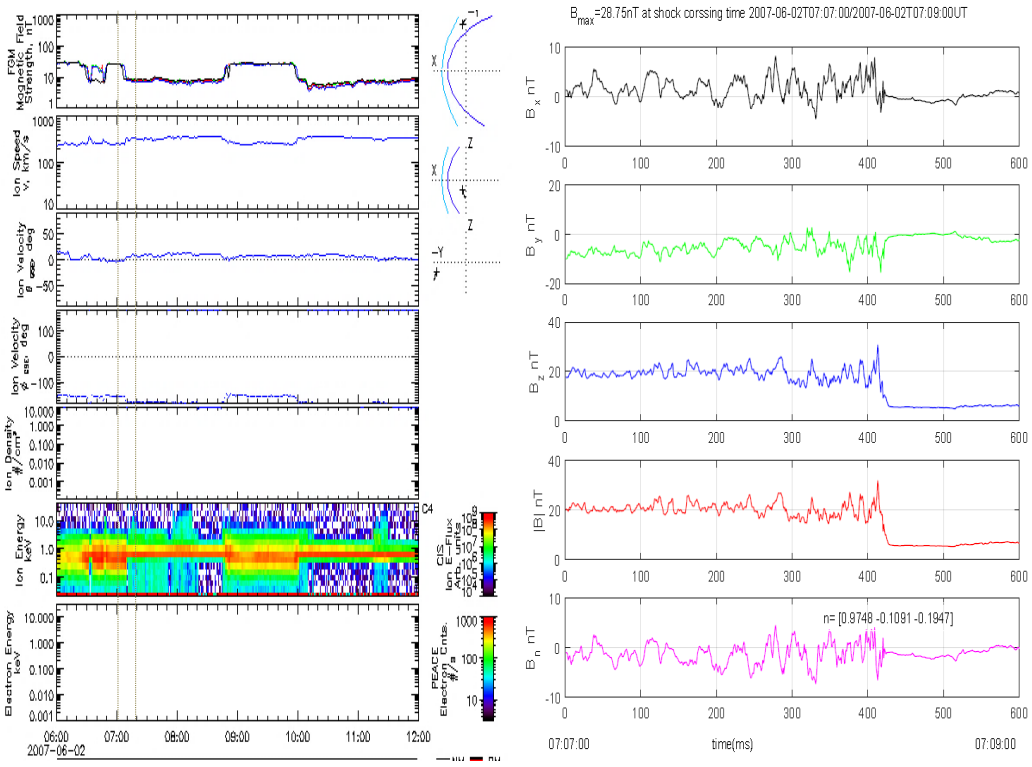

Figure 18: The measurement of the magnetic field (FGM), ion density, ion velocity, ion energy, and electron energy, B-wave frequency, E-wave frequency are shown on the left side of the image from top to bottom correspondingly. The magnetic field three component average value measured by MVA PPS method is also shown. The polarised magnetic field components are $B_x \simeq 0.51$ nT$B_y \simeq 1.09$ nT, $B_z \simeq 5.9$ nT. The magnetic field $B_{am} \simeq 6.03$ nT in foot region and maximum magnitude increases up to $B_{max} \simeq 28.75$ nT across ramp transition at shock crossing time. B-field to shock normal angle $\theta_{Bn} \simeq 82.98$ and shock normal (n) $\simeq (0.9748, -0.1091, -0.1947)$ as shown in right hand side. These values corresponds to the measurements between 2007-06-02 T07:07:00 - 2007-06-02 T07:09:00UT.

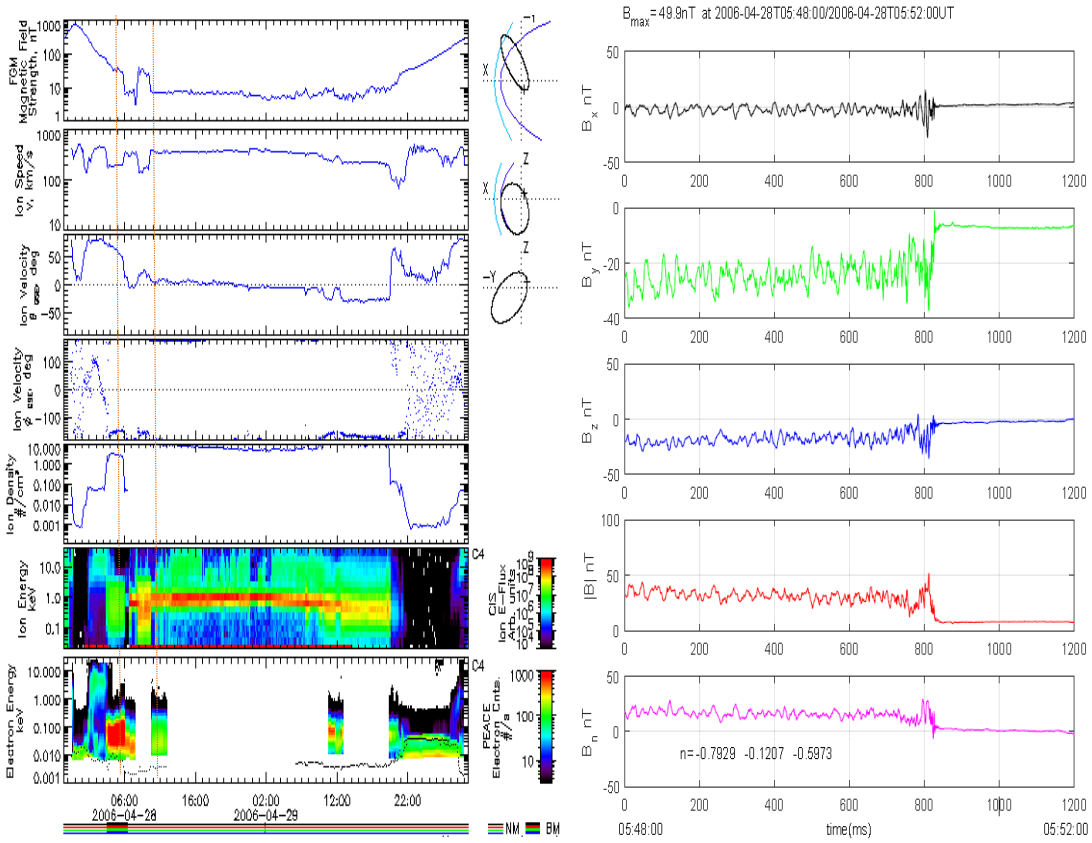

Figure 19: The measurement of the magnetic field (FGM), ion density, ion velocity, ion energy, and electron energy, B-wave frequency, E-wave frequency are shown on the left side of the image from top to bottom correspondingly. Magnetic ramp transition region in QPS front measure average value of the magnetic field components are $B_x \simeq 2.31$ nT, $B_y \simeq 7.05$ nT, $B_z \simeq 2.37$ nT. Time: 2006-04-28 T05:48:00 - 2006-04-28 T05:52:00UT. The magnitude of the magnetic field $B_{am} \simeq 8.04$ nT in foot region and maximum magnetic field magnitude increases up to $B_{max} \simeq 49.9$ nT across ramp transition at QPS front. These values corresponds to the measurements between 2006-04-28 T05:48:00 - 2006-04-28 T05:52:00UT.

Computed Alfvén velocity at the QPS front region on 16-02-2015 at 11:08:00UT is $v_A \simeq 42.2$ km/s. Alfvén velocity variation rates is rely on B_x, B_y, B_z surface magnetic field and electron plasma particles density n_e perturbation in ramp $\frac{\delta B}{B_0}$ transition region in QPS front in resistive Earth magnetic field line boundary surface region. In ramp region of QPS front the average magnetic field components are $B_x \simeq 5.58$, $B_y \simeq 6.16$ nT, $B_z \simeq 5.03$ nT as shown Figure 9. These values were measured using PPS real time MVA method. Alfvén resonance occurs at magnetic field magnitude $B_{max} \simeq 59.35nT$ in ramp region of QPS front as shown in the middle part of Figure 9 at 16-02-2015 T11:10:30UT.

The Earth magnetopause resistive magnetic field line boundary surface layer transition region finite average magnetic strength $|B| \simeq 8.7nT$ and electron plasma mass density $n_e \simeq 23.5cm^{-3}$ were measured on 6-02-2015 T11:08:00UT. Corresponding Alfvén velocity is $v_A \simeq 42.2km/s$. Alfvén velocity $v_A \simeq 49.14km/s$ also measured on 01-03-2012 T11:25:00UT. All other values of Alfvén velocity v_A for the period 2001 - 2015 are listed in Table-3.

4.4.1 Electron plasma particles velocity measurement

An electron plasma charge particles planar polarised propagating wave in 3D velocities space v_x, v_y, v_z induces motion variation in ramp region of QPS front at each upstream magnetic field to wave propagation angle θ_{Bk} within finite range $45 \leq \theta_{Bk} \leq 90$. Electron plasma charge particles motion variation in ramp region measured within N points spread real time 3D space precise positioning average value at QPS transition time using HIA data numeric computation operation real time velocities measurement method.

$$\bar{v_x} = \frac{1}{N}\Sigma_{i=1}^{N} v_x^i,$$

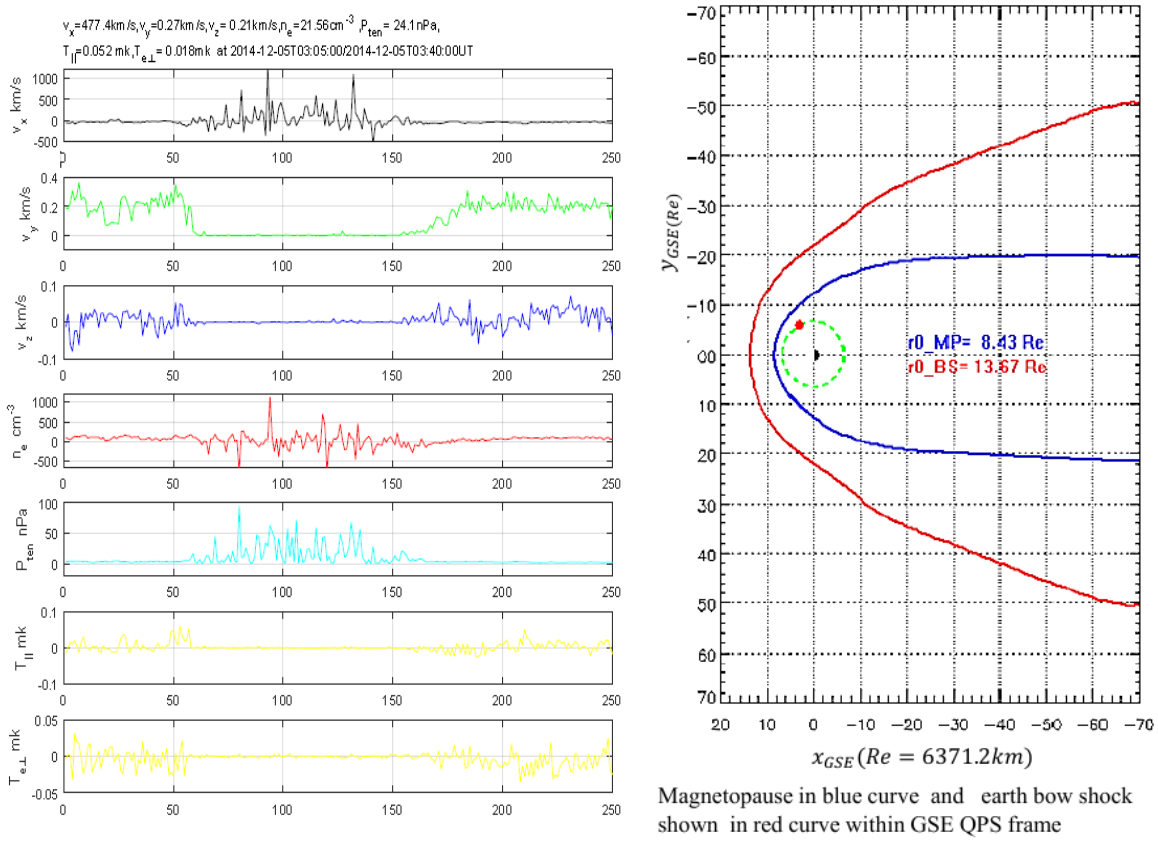

Figure 20: Electron plasma density perturbation and other parameters measured at QPS front on 2014-12-05 T03:05:00UT.

$$\bar{v_y} = \frac{1}{N}\Sigma_{i=1}^{N} v_y^i,$$

$$\bar{v_z} = \frac{1}{N}\Sigma_{i=1}^{N} v_z^i.$$

An average measured electron plasma particles velocities values in ramp region in of QPS are: $v_x \simeq 477.4$ km/s, $v_y \simeq 0.27$ km/s and $v_z \simeq 0.21$ km/s as shown in Figure 20 at date/time 2014-12-05 T03:05:00UT.

4.4.2 Electron plasma particles density measurement

An ions, electron plasma particles density perturbation from $15.23R_E$ resistive bow shock accelerates ions, electron plasma particles towards sunward side $10.05R_E$ resistive magnetopause magnetic field region. Two stream speed difference between slow and fast induce quasi parallel shock at $10.02R_E$ magnetosheath region at angle between shock normal and magnetic field $\theta_{Bn} \simeq 23.3$ on time 2015-04-26 T11:02:00UT partially consistent to (Balikhin, 2003, Matsukiyo & Scholer, 2012). The ion kinetic energy fraction transforms into thermal resistivity in downstream doubling magnetic field thickness barrier and increasing electron plasma thermal flux into upstream direction magnetic field surface. As a result, resistive outermost magnetopause magnetic field line l_n surface induces resistive QPS wave.

Sunward side $10.05R_E$ of Earth magnetopause resistive Earth magnetic field line boundary surface layer QPS wave dispersion variation rates compress upstream electron plasma particles density n_e. Electron plasma particles density n_e variation induces perpendicular pressure $P_{e\perp}$. As a result, e-plasma viscous and thermal resistivity variation occurs on elliptically polarised B_x, B_y, B_z surface in ramp region at each angle between shock normal and upstream magnetic field within finite range $45 \leq \theta_{Bn} \leq 90$. QPS wave surface thermalised electron plasma density n_e variation at each θ_{Bn} with time within N points spread measured average value at several dates between 2001-2015.

An electron plasma particles density n_e variation average value measurement in QPS front ramp region finite forward N time series scale step t_n generalised as

$$\bar{n_e} = \frac{1}{N} \Sigma_{i=1}^{N} n_e^i.$$

QPS wave compress electron plasma particles density $n_e \simeq 23.5 cm^{-3}$ variation in ramp region in shock front numerically computed within 2^{nd} order perturbation at

$10.05R_E$ Earth magnetopause magnetic line boundary surface layer at angle between shock shock normal and upstream magnetic field $\theta_{Bn} \simeq 59.39$ on time 16-02-2015 T11:08:00UT.

But equipartition $T_{\parallel}$, $T_{e\perp}$ energy distribution problem arises in magnetic ramp transition region partially consistent with (Balikhin, 2014, Burch et al., 2016, Matsukiyo & Scholer, 2012). An electron plasma particles density value $n_e \simeq 12.9cm^{-3}$ variation on elliptically polarised $B_x \simeq 18.5nT$, $B_y \simeq 9.25nT$,$B_z \simeq 6.41nT$ in ramp $\frac{\delta B}{B_0} \simeq 2.26nT$ region at QPS front ramp region induce plasma particles pressure tension $P_{ten} \simeq 24.1$ nPa, parallel temperature $T_{i\parallel} \simeq 0.065MK$, perpendicular temperature $T_{e\perp} \simeq 0.01MK$ variation in ramp $\frac{\delta B}{B_0} 2.26nT$ region in QPS front.

An electron plasma particles density average value $n_e \simeq 10.05cm^{-3}$ measured at temperature $T_{e\perp} \simeq 0.018$MK at QPS wave upstream surface as shown in Figure 20 on 2014-12-05 T03:05:00UT

The complete electron plasma density measurements for 2001 - 2015 are listed in Table 2

4.4.3 Measurements of the ion and electron plasma pressure variations

Parallel ion plasma particles pressure $P_{\parallel}$ and electron plasma particles perpendicular pressure $P_{e\perp}$ variations with time changes direction of the wave propagation within angle between shock normal and upstream magnetic field θ_{Bn} in sunward side $10.05R_E$ Earth magnetopause layer. Ion plasma particles parallel $P_{i\parallel}$, perpendicular $P_{e\perp}$ pressure and tenser P_{ten} variation with time at elliptically polarised magnetic field B_x, B_y, B_z in ramp transition region within N points spread measured average value within 1^{st} up to n^{th} order QPS frame transition within satellite separation vector R_1, R_2, R_3 at arc length scale s_1, s_2, s_3 in time scale step t_n classified as:

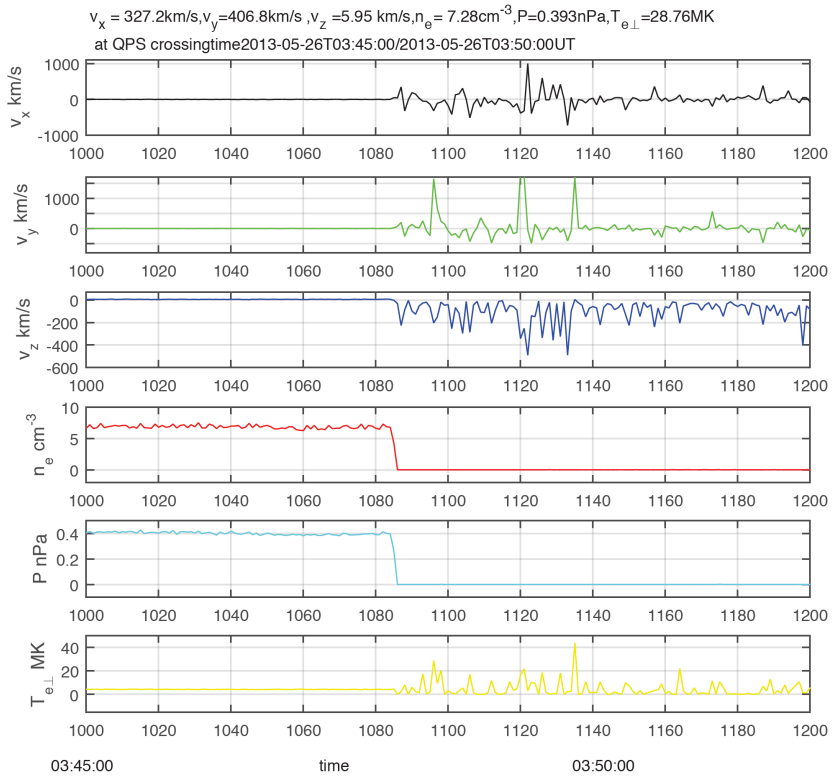

Figure 21: Shock normal velocity components $v_x \simeq 327.2$ km/s, $v_y \simeq 406.8$ km/s and $v_z \simeq 5.95$ km/s. Electron plasma particles density $n_e \simeq 7.28\ cm^{-3}$ $P_{e\perp} \simeq 0.393$ nPa, temperature $T_{e\perp} \simeq 28.76$ MK. Shock normal velocity $v_n \simeq 91.79$ km/s, Alfvén velocity $v_A \simeq 88.33$ km/s measured at 2013-05-26 T03:45:00UT

$$\bar{P_{i\|}} = \frac{1}{N}\Sigma_{i=1}^{N} P_{\|}^{i},$$

$$\bar{P_{e\perp}} = \frac{1}{N}\Sigma_{i=1}^{N} P_{e\perp}^{i},$$

$$\bar{P_{ten}} = \frac{1}{N}\Sigma_{i=1}^{N} P_{ten}^{i}.$$

Upstream e-plasma particles density $n_e \simeq 5.31cm^{-3}$ variation induces perpendicular pressure $P_{e\perp}$ ≃0.021nPa on elliptically polarised magnetic field $B_x \simeq 2.74nT$, $B_y \simeq 1.74nT, B_z \simeq 7.38nT$ surface. In ramp region the real time precise positioning HIA computed is shown in Figure 22 for the date/time 2012-03-01 T03:42:00UT.

4.4.4 Eigen mode eigen value variation classification

QPS wave dispersion relation changes k-wave numbers non-linear wavelength λ at each angle between wave propagation and upstream magnetic field θ_{Bk} in ramp region of QPS front at $10.05R_E$. But, k-wave numbers wavelength λ variation detection problem arises within group wave velocities v_{ge} in ramp region in QPS front at Earth radial distance $10.05R_E$ (Balikhin, 2014, Burch et al., 2016, Matsukiyo & Scholer, 2012, Wilson, 2013).

Thermal kinetic ions q_i cyclotron wave and upstream gyro radial electron plasma charge particles q_e wave propagation time dependent eigen value in eigen function mode k_{eig}, $\Psi_E(x, y, z, t)$ variation is classified in ramp region at QPS front in resistive Earth magnetic field boundary surface. Kinetic ion cyclotron wave energy and upstream gyro radial electron plasma 3D wave propagation energy variation with temperature $T_{\|}$, $T_{e\perp}$ in velocities space in QPS front ramp region quantised as eigen value of k-wave numbers in eigen mode k_{eig}, $\Psi_E(r_{el}, \theta_{Bk}, t$. Highly thermalised electron plasma charge particles q_e speed remains higher then planar polarised electron plasma 3D wave propagation speed in QPS front ramp transition region.

Upstream stream QPS wave surface propagating k-wave numbers wavelength λ vari-

ation in 3D velocities space v_x ,v_y, v_z in ramp region with angle between wave propagation and upstream magnetic field $45 \leq \theta_{Bk} \leq 90$ is quantised into three different wave mode as :

- Minimum wave number k_{min} wave length λ_{min} variation at low θ_{Bk} in shock front foot region;
- Maximum k-wave number k_{max} wavelength λ_{max} variation within $45 \leq \theta_{Bk} \leq 90$ in ramp transition region;
- Intermediate wave number k_{int} wave length (λ_{int}) variation in QPS front ramp transition region within angle between shock normal and upstream magnetic field finite range $45 \leq \theta_{Bn} \leq 90$.

QPS wave dispersion relation changes non-linear wavelength of the slow, fast and intermediate k-wave numbers with each angle between direction of the k-wave propagation and upstream magnetic field θ_{Bk} generalised as:

$$\lambda_{min} \simeq \frac{2\pi}{k_{min}} \simeq \frac{\omega_{pe1}}{v_{phe1}};$$

$$\lambda_{max} \simeq \frac{2\pi}{k_{max}} \simeq \frac{\omega_{pe2}}{v_{phe2}};$$

$$\lambda_{int} \simeq \frac{2\pi}{k_{int}} \simeq \frac{\omega_{pi}}{v_{ph}}$$

Eigen value classified on the bases of the propagating waves minimum wavelength λ_{min} variation in foot region and maximum wavelength λ_{max} variation in upstream magnetic field in QPS front ramp region. Eigen value of the intermediate k-wave number is classified within intermediate wavelength λ_{int} variation in ramp $\frac{\delta B}{B_0}$ region in QPS front with angle between shock normal and upstream magnetic field $45 \leq \theta_{Bn} \leq 90$.

Non-linear wavelength variation with time ratio $10 \leq \frac{\lambda_{max}}{\lambda_{int}}$ in QPS front ramp is classified planar, elliptical polarisation with variation rates of each angle between direction of the wave propagation and upstream magnetic field θ_{Bk}.

4.4.5 Ions and electron plasma particles temperature measurement

1^{st} up to n^{th} order of QPS wave e-plasma temperature variation within satellite separation vector R_1, R_2, R_3 at elliptically polarised arc length scale s_1, s_2, s_3 in finite forward time series scale step t_n can be calculated as :

$$\bar{T_{e\perp}} = \frac{1}{N}\Sigma_{i=1}^{N} T_{e\perp}^{i}.$$

H^{+1}, H_e^{+2} ion plasma particles temperature variation measurement in N points are:

$$\bar{T_{i\parallel}} = \frac{1}{N}\Sigma_{i=1}^{N} T_{i\parallel}^{i},$$

Each phase space electron plasma particles parallel temperature $T_{\parallel} \simeq 0.7KM$, perpendicular temperature $T_{e\perp} \simeq 1.1MK$ at time 2012-03-01 T03:42:00UT are shown in Figure 22.

Thermalise ions temperature $T_{i\parallel} \simeq 0.75$MK increasing in magnetic ramp $\frac{\delta B}{B_0} \simeq 5.09nT$ region in QPS front at date/time 01-03-2012 T03:42:00UT. QPS front magnetic ramp $\frac{\delta B}{B_0} \simeq 5.09nT$ region magnetic strength $|B| \simeq 8.06$ nT variation with temperature $T_{\parallel} \simeq 0.75MK$,$T_{\perp} \simeq 1.14MK$ measured within angle between shock normal and upstream magnetic field $\theta_{Bn} \simeq 84.4$ as shown in Figure 22 at time 01-03-2012 T03:42:00UT. Shock normal measured value $n_x \simeq 0.8930$, $n_y \simeq 0.1048$, $n_z \simeq 0.4288$ at date/time 01-03-2012 T03:42:00UT. e-shock current density is increasing into ramp region region. Shock normal magnetic field $B_n \simeq 5.85$ nT changes in ramp transition region as shown in Figure 22 at date/time 2012-03-01 T03:42:00 - 2012-03-01 T03:47:00UT. Main issue is emitted protonic wave changes thermal resistivity at elliptically polarised magnetic field $B_x \simeq 2.74nT, B_y \simeq 1.74nT, B_z \simeq 7.38nT$ surface magnetic wave frequency 0.01 Hz up to 1kHz variation occurs. Temperature varia-

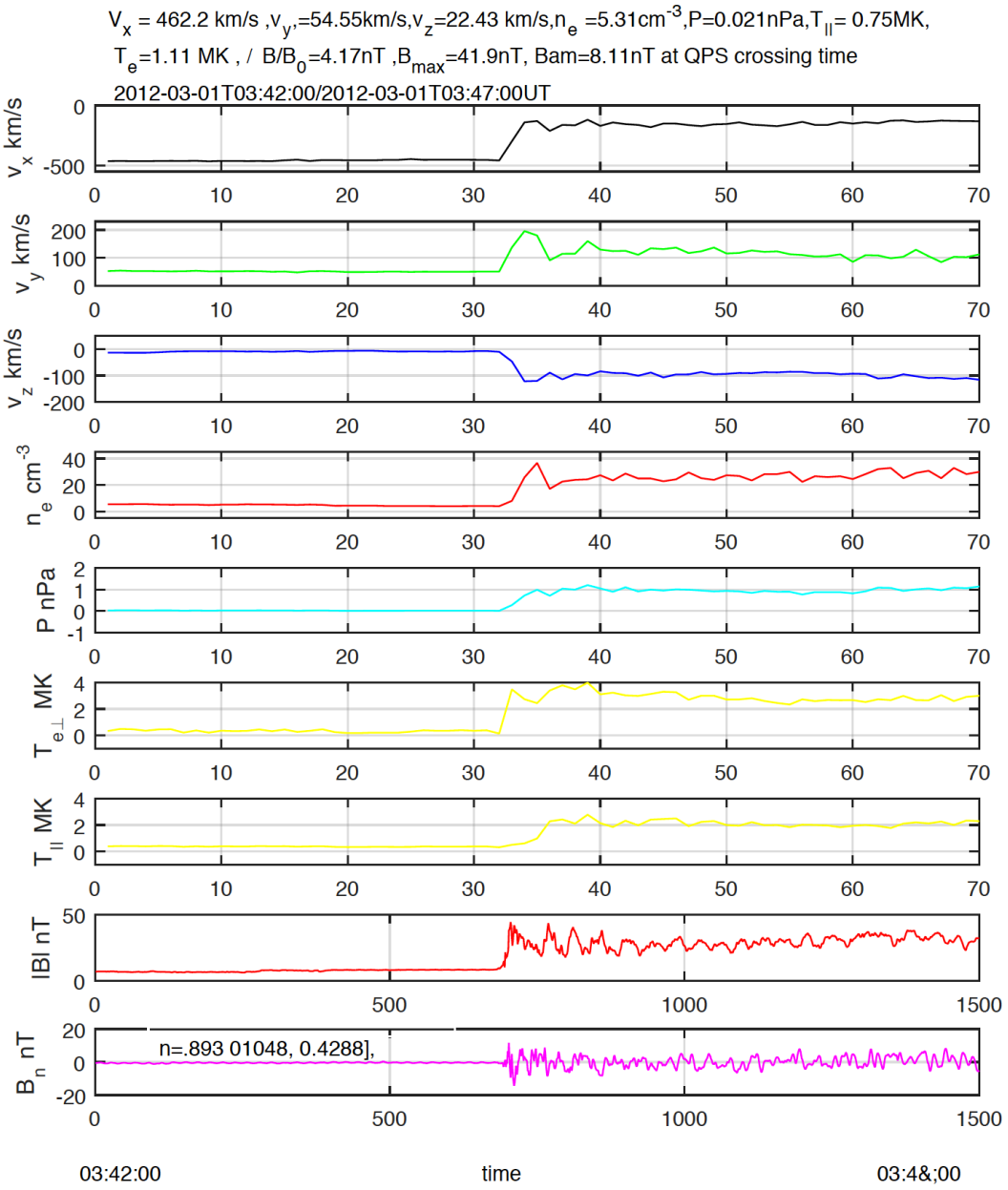

Figure 22: QPS parameters measured at 2012-03-01T03:42:00UT. The values at crossing time are shown on top of the figure.

tion is changes upstream electron plasma power spectral energy and downstream ions power spectral energy in ramp region. As a result, intensity variation induces discrete resolution differs at each phase space in ramp $\frac{\delta B}{B_0}$ region at QPS transition time classified in to CIS energy-time spectrogram. An electron plasma particles temperature $T_{e\perp}$ is decreases after emitting protonic wave energy, as a result, 3D velocities decreasing with θ_{Bk}. Non-equipartition e-plasma particles temperature $T_{\parallel} \simeq 1.49MK$ and $T_{e\perp} \simeq 2.35MK$ measured into ramp $\frac{\delta B}{B_0} \simeq 3.96nT$ region in QPS front at day/time 2012-03-01 T03:13:00UT. An electron plasma particles temperature variation ratio $\frac{\delta T_{e\perp}}{T_{\parallel}} \simeq 1.57$MK in ramp $\frac{\delta B}{B_0} \simeq 3.96nT$ in QPS front measured at day/time 2012-03-01 T03:13:00UT.

4.5 QPS normal velocity measurement method

Shock normal velocity v_n subcomponent v_x, v_y, v_z variation occurs with angle between wave propagation and upstream magnetic field θ_{Bk} from sunward side $15.23R_E$ resistive Earth bow shock to earth radial distance $10.05R_E$ compress earth magnetopause resistive magnetic field line l_n, l_{n-1}, l_3, l_2, l_1 boundary surface layer transition region. Shock normal velocity v_n sub component upstream electron plasma gyro-radial motion variation with time into 3D velocities space v_x, v_y, v_z in ramp $\frac{\delta B}{B_0}$ region in QPS within each angle between wave propagation and upstream magnetic field $45 \leq \theta_{Bk} \leq 90$ measured average value using HIA 3D virtual space real time precise positioning computation method. Shock normal vector n_x, n_y, n_z variation at elliptically polarised magnetic field B_x, B_y, B_z surface in ramp region at QPS transition time measured value using MVA numeric computation operation method. 2^{nd} order perturbation at sunward side Earth radial distance $10.05R_E$ in compress earth magnetopause resistive Earth magnetic field line boundary layer surface transition region real time precise positioning shock normal velocity v_n numeric computation equation generalised as:

$$v_n = \bar{v_x} n_x + \bar{v_y} n_y + \bar{v_z} n_z.$$

The sunward side $15.2R_E$ Earth bow shock to $10.05R_E$ earth magnetopause resistive magnetic field line boundary surface layer ramp region in QPS front real time precise positioning shock normal velocity $v_n \simeq 238.8$ km/s variation rates calculated on 16-02-2015 at 11:08:00UT. QPS transition time series scale, shock normal velocity v_n at the ramp region are shown in Table 3.

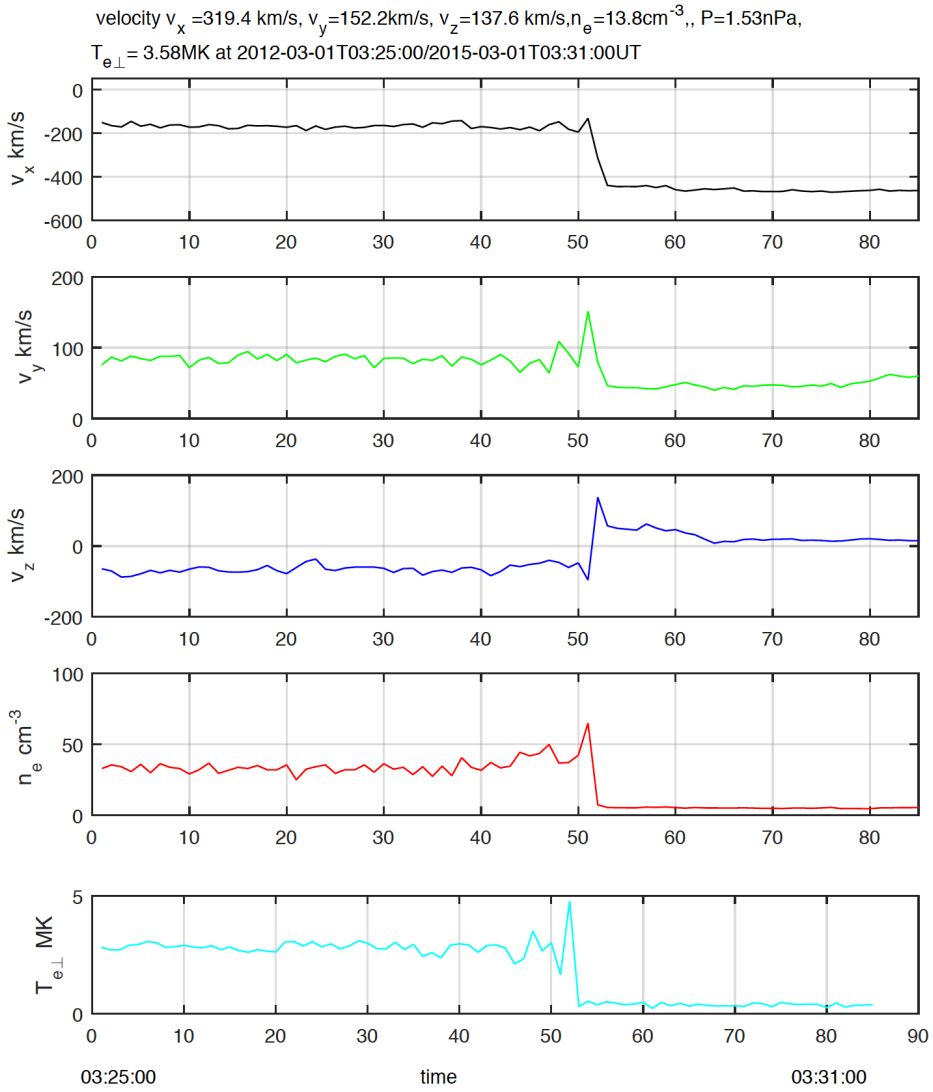

Figure 23: QPS normal velocity components v_x, v_y, v_z measured values on 2012-03-01 T03:25:00UT. From top to bottom: Planar polarised e-plasma gyro radial motion variation average value in 3D velocities space at angle between wave propagation and upstream magnetic field and thermalised electron plasma temperature variation.

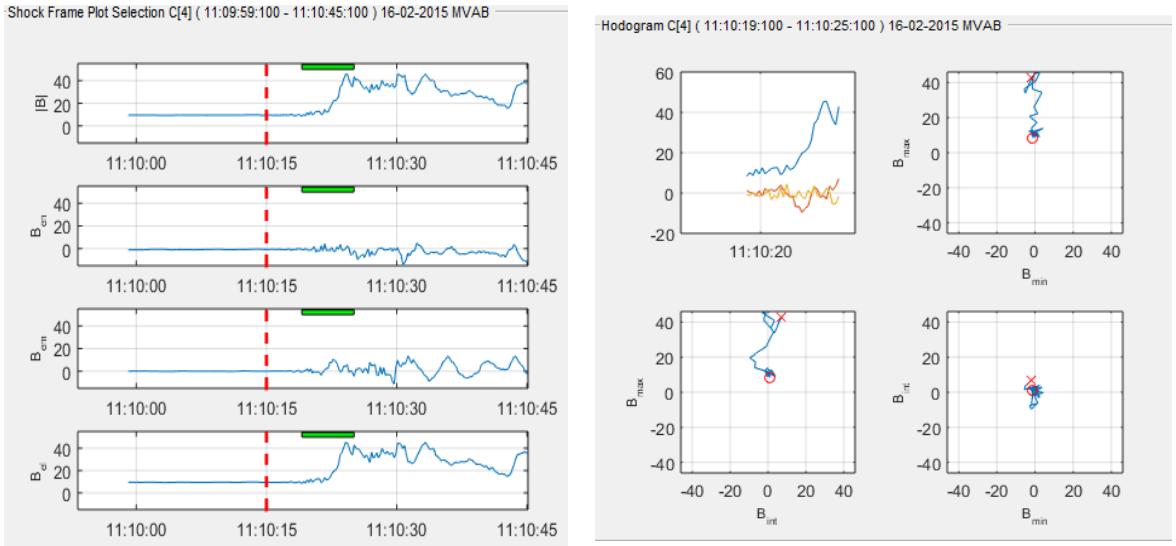

Figure 24: The shock hologram in right hand side of the figure within angle between shock normal and upstream magnetic field (θ_{Bn}) $\simeq$ 77.268, shock normal $\simeq$ (0.83036, -0.43343, 0.3502) on 16-02-2016 at 13:02:24:042:00UT. Paredu model method detected shock normal angle $\theta_{Bn} \simeq 77.26$, shock normal $\simeq$ (0.83036, -0.43343, 0.3502). Paredu model based detected angle between shock normal and upstream magnetic field θ_{Bn} and shock normal (n) value is compared with real time cluster precise positioning satellite navigation system (PPSNS) data numeric computationally measured value.

4.6 Summary

Real time precise positioning direction of wave propagation and shock normal variation in ramp region in QPS front measured at sunward Earth radial distance $10.05R_E$ compress Earth magnetopause resistive magnetic field boundary surface transition region. QPS crossing time upstream e-plasma particles power spectral energy density, and reflective downstream ions plasma power spectral energy density variation in QPS front ramp region induces discrete resolution of the H^+ and electron discretised into energy-time spectrogram. 2^{nd} order perturbation at earth radial distance $10.05R_E$ compress Earth magnetopause resistive magnetic field boundary surface induces magnetic field variation into ramp region within angle between shock normal and upstream magnetic field finite range $45 \leq \theta_{Bn} \leq 90$ in QPS front. QPS shock normal velocity v_n and Alfvén velocity in ramp $\frac{\delta B}{B_0}$ region with angle between shock normal and upstream magnetic field $45 \leq \theta_{Bn} \leq 90$ measured at several different times between 2001 - 2015.

5 Collisionless QPS Mach number measurements

At sunward side $15.23R_E$ resistive Earth bow shock to Earth radial distance $10.05R_E$ compress magnetopause magnetic 2^{nd} order perturbation in resistive field curvature lines l_n, l_{n-1}, , , l_3, l_2, l_1 boundary surface layer form ramp in QPS front. But ramp transition region induce shock normal velocity v_n and Alfvén velocity variation within angle variation between shock normal and upstream magnetic field θ_{Bn}. Shock normal velocity v_n to Alfvén velocity variation numeric computation operation gives real time precise positioning Mach number measurement equation classified as:

$$M = \frac{v_n}{v_A}.$$

If injected shock wave energy is increases then plenary polarised electrons plasma

gyro-radial motion variation components v_x, v_y, v_z along with shock normal n_x, n_y, n_z increases across elliptically polarised B_x, B_y, B_z surface guided path. A direction of the wave propagation changes with shock normal(n_x, n_y, n_z) within 3D planar polarised velocities space v_x, v_y, v_z in ramp region in QPS front at sunward side $10.05R_E$ Earth magnetopause resistive each magnetic field line boundary surface layer transition region.

As a result shock normal velocity v_n increasing but transverse Alfvén velocity v_A decreasing at sunward side of Earth radial distance $8.43R_E$ up to $10.05R_E$ and compress Earth magnetopause resistive magnetic field line l_n, l_{n-1}, , , l_3, l_1 boundary surface layer.

QPS wave transition time induce 2^{nd} order perturbation in resistive Earth magnetic field at Earth radial distance $10.05R_E$ compress Earth magnetopause region precise positioning real time Mach number (M) $\simeq 6.1$ measured in ramp $\frac{\delta B}{B_0} \simeq 3.9$ nT transition region of QPS front at angle between shock normal and upstream magnetic field $\theta_{Bn} \simeq$ 59.39 on date/time 16-02-2016 T11:08:00UT. Mach number variation in ramp $\frac{\delta B}{B_0}$ region within QPS transiting time measured at sunward side $10.05R_E$ of Earth magnetopause were measured between 2001 - 2015 and listed in Tables 1 - 4. If data is not available then variation rate of the Mach number measured value can be also used for proximation of shock variables parameters.

5.1 Summary

Magnetised electron plasma particles viscous resistivity and ion plasma particles thermal resistivity variation occurs in QPS front ramp region at Earth radial distance 10.05 R_E. Solar wind ta sunward Earth radial distance$10.05R_E$ compress earth magnetopause magnetic field which leads to the increasing of the angle between shock normal and upstream magnetic field θ_{Bn} which was evaluated at several different date/times between 2001-2015. QPS parameter known as mach number (M) is listed into Table 1 for all these measurements.

Mach number (M) variation in ramp region is directly linked with direction of the propagating wave which carry plasma particles mass momentum and energy from $10.05R_E$ Earth magnetopause resistive magnetic field to $10.02R_E$ magnetosheath transition region. But plasma particles mass momentum and energy injection variation rates differ from northward side polar cusp region to plasmapause and plasmasphere at low latitude boundary layer. As a result, van allen radiation belt: A at 12000 km and radiation belt: B at 4000 km region high electron plasma stream line flow induces chorus wave. A low attitude ionosphere region ultraviolet rays is ionised hydrogen H^+, helium H_e^{+2} oxygen O^{-2}. As a result, ionosphere compression and non-linear sun synchronised polar orbit region resistive e-shock current j_e direction variation occurs at resistive Low Latitude Boundary (LLB) layer. LLB layer ions and electron plasma particles density n_e, n_i perturbation induce pressure $p_{\parallel}$, $p_{\perp}$ and temperature $T_{\parallel}$, $T_{\perp}$ variation. Ions, electron plasma particles 3D velocities space v_x, v_y, v_z turbulence flow variation in QPS front ramp region changes space weather.

6 QPS measurements based on multi-parameters correlation classification method

Quasi Perpendicular Shock parameters are known as: magnetic ramp $\frac{\delta B}{B_0}$, mach number (M), angle between shock normal and upstream magnetic field θ_{Bn}, Paredu mach number M_P, Paredu upstream magnetic field to shock normal angle θ_{Bn_P} QPS parameters identification is discussed below.

6.1 Correlation of the angle between shock normal and upstream magnetic field and Mach number.

Each angle variation between shock normal and upstream magnetic field within finite range $45 \leq \theta_{Bn} \leq 90$ is a function of the Mach number (M) measured value correlated within Earth magnetosphere subdomain transition region. Blue line curve represents the angle variation between shock normal and upstream magnetic field as function of the Mach number (M) in magnetic field of the Earth magnetosphere at low plasma β as shown in Figure 25. QPS changes from stationary to non-stationary at high mach number in resistive earth magnetic field curvature line l_n, l_{n-1}, , , , l_2, l_1 inner boundary surface in sunward magnetosphere subdomain transition region.

Each upstream magnetic field to shock normal angle variation rates with time within finite range $45 \leq \theta_{Bn} \leq 90$ is a function of the Paredu Mach number (M_P) measured value proximately correlated. Blue line polynomial curve represents Paredu Mach number M_P and correspond to angle variation between shock normal of upstream magnetic field θ_{Bn} at low plasma β as shown in Figure 26. Each angle between shock normal and upstream magnetic field θ_{Bn} variation is a function of the Paredu Mach number (M_P) measure value. Blue line represent dependance of the angle between shock normal and upstream magnetic θ_{Bn} variation as a function of the Paredu Mach number M_P at low plasma β.

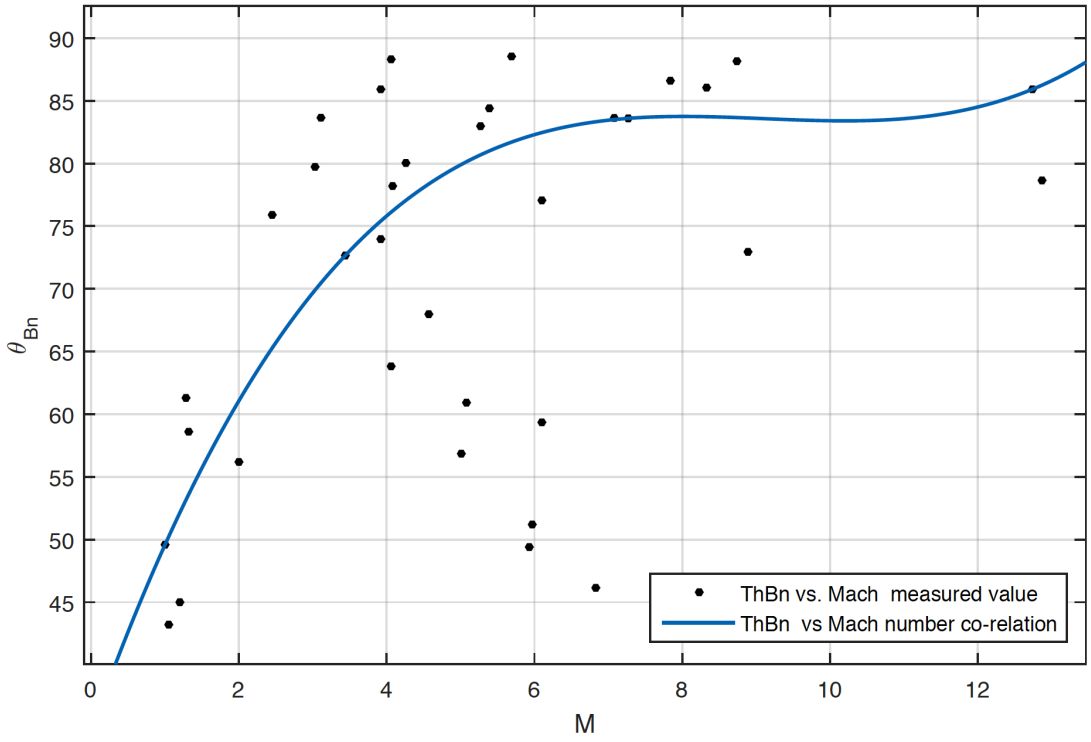

Figure 25: Each black dot represents the angle between shock normal and upstream magnetic field θ_{Bn} and the Mach number (M) real time precise positioning measured value at specific time and date. The Blue line curve plot shows correlation of the QPS parameters known as angle between shock normal and upstream magnetic field θ_{Bn} with Mach number (M) in magnetic ramp transition region at QPS front.

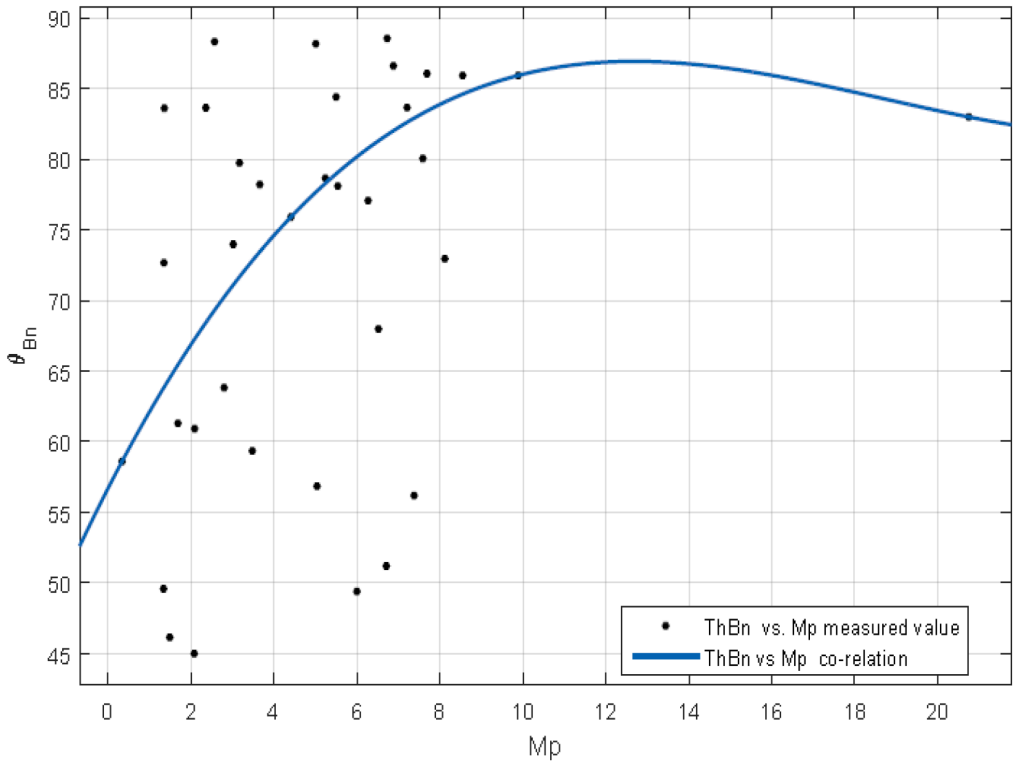

Figure 26: The angle between shock normal and upstream magnetic field θ_{Bn} and Paredu Mach number M_P measured value by theoretical Paredu model. Black dot correspond to the angle between shock normal and upstream magnetic field θ_{Bn} co-related to the Paredu Mach number M_P. The Blue plot line corresponds to the co-relation of the QPS as angle between shock normal and upstream magnetic field and Paredu Mach number M_P variation in the Earth magnetic ramp $(\frac{\delta B}{B_0})$transition region. Blue line plot provides evidence about angle variation between shock normal and upstream magnetic field θ_{Bn} is a function of the Paredu Mach number M_P.

Table 1: Collisionless shock parameters. Measured values.

No	dd:mm:yy	Start Time	End Time	M	$\frac{\delta B}{B_0}$	θ_{Bn}	M_P	θ_{BnP}	P_{ten}	$P_{\parallel}$	$T_{\parallel}$	$T_{e\perp}$
1	16:02:2015	11:08:00	11:13:00	5.2	3.9	59.35	4.22	61.3			2	
2	05:12:2014	03:05:00	03:40:00	1.28	2.26	45	2.08	52.1	24.1		0.05	0.01
3	27:11:2014	04:05:00	04:15:00	3.7	2.53	86.8	3.16	81.74				
4	11:01:2014	22:51:00	22:56:00	5.1	4.2	60.92	9.16	71.56				
5	11:01:2014	22:51:00	22:56:00	5.08	3.61	60.6	2.08	71.56				
6	26:05:2013	08:45:00	08:47:00	1.87	2.73	80.35	0.34	52.34	0.39			28.8
7	16:05:2013	03:52:00	03:54:00	5.89	4.79	78.09	5.54	87.99	4			17.76
8	02:06:2012	16:36:00	16:38:00	3.03	3.4	79.7	3.17	83.48	0.18		0.42	
9	01:03:2012	03:13:00	03:17:00	9.25	3.96	81.64	8.12	81.64	0.94		1.49	2.35
10	01:03:2012	03:18:00	03:24:00	6.1	6.1	5.48	77.06	6.67	86.89			
11	24:01:2012	03:58:00	04:00:00	2.27	5.27	68.52	2.93	74.91	0.48		1.15	4.2
12	01:03:2012	03:25:00	03:31:00	4.06	7.34	88.31	2.57	87.99	1.53			3.58
13	01:03:2012	03:42:00	03:47:00	5.19	5.09	89.4	5.46	84.93	0.02		0.75	1.11
14	24:01:2012	03:58:00	04:00:0	3.17	5.27	83.64	7.21	74.34	0.48		1.149	4.2
15	30:12:2011	03:03:45	03:05:00	3.64	3.37	73.97	3.03	87.64	0.52			2.42
16	30:12:2011	04:21:00	04:26:00	4.11	7.42	80.04	7.6	88.21	0.72		1.5	1.91
17	30:03:2011	14:21:00	14:24:20	1.06	1.35	39.2	1.49	52.46	0.06			3.87
18	15:02:2011	09:18:00	09:23:00	6.83	6.36	85.5	7.38	44	0.33	0.3	7.99	3.23
19	27:05:2010	02:28:00	02:33:00	4.16	3.78	56.86	5.08	63.63	0.035	0.36	0.2	0.28
20	25:05:2010	05:16:00	05:18:00	9.62	3.49	77.6	6.87	86.19	0.036	0.23	0.06	0.18
21	21:01:2010	08:37:00	08:39:00	7.8	6.15	86.66	8.54	88.78	0.491		3.08	4.87
22	20:05:2009	20:16:30	20:18:30	3.91	2.75	85.92	5.24	89.6	0.138		1.102	1.11
23	07:06:2008	12:16:30	12:17:40	12.61	7.39	78.65	9.9	66.07	0.30		1.65	1.36
24	02:06:2007	07:07:00	07:09:00	5.28	3.8	82.99	2.36	76.8	0.91	0.9	0.946	1.24
25	07:05:2007	08:27:00	08:29:00	7.08	5.1	83.6	9.06	39.94	0.06	0.032	o.08	0.09
26	28:04:2006	05:48:00	05:52:00	5.97	5.21	51.2	6.72	69.46	0.035	0.020	0.155	0.31
27	20:04:2005	05:05:00	05:07:00	4.06	2.8	63.82	2.8	78.76	1.25	0.83	1.28	4.04
28	04:04:2004	08:57:00	09:02:00	1.28	1.5	61.3	1.69	54.3	0.03		0.47	0.78
29	12:06:2003	06:05:00	06:07:00	1.01	2.9	49.59	1.35	57.2	0.056	0.073	22.75	20.41
30	23:05:2002	01:15:00	01:20:00	4.09	6.84	78.2	3.86	68.9	1.33	1.03	1.23	1.97
31	20:05:2002	03:40:00	03:45:00	5.93	2.168	49.4	5.99	57.8	0.13	0.079	0.26	0.6
32	16:05:2003	03:52:00	03:54:00	5.05	4.79	85.6	9.16	87.99				
33	03:05:2002	08:10:00	08:15:00	4.57	3.97	67.98	6.52	85.24	0.094	0.039	0.7	1.3
34	20:05:2002	03:40:00	03:45:00	1.96	2.17	54.73	2.67	57.8				
35	17:01:2001	06:33:00	06:36:00	5.69	6.56	88.54	6.73	83.83				
36	17:01:2001	06:33:00	06:36:00	2.47	4.55	87.5	0.57	83.0				

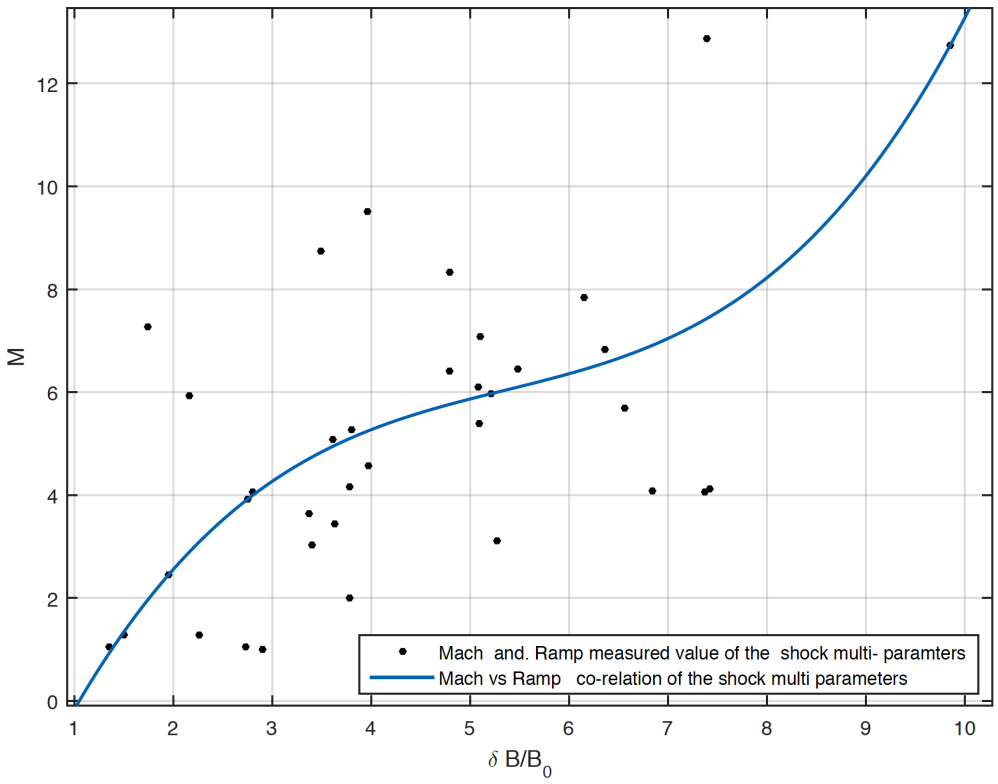

Figure 27: Magnetic ramp $\frac{\delta B}{B_0}$ measured value as a function of the Mach number (M) measured value at low plasma β.

6.2 The magnetic ramp and Mach number correlation

QPS parameters known as magnetic ramp $\frac{\delta B}{B_0}$ and Mach number (M) are shown as black dots on the Figure 27. The probabilistic curve (shown in a blue colour) represents variation rate of the Earth magnetic ramp $\frac{\delta B}{B_0}$ as function of the Paredu Mach number M_P for the case of low plasma β (see Figure-28). Blue polynomial probabilistic curve plot represents variation rates of the Earth magnetic ramp ($\frac{\delta B}{B_0}$) as a function of the Mach number M at low plasma β as shown in Figure-29. This real time dependent value compared with theoretically calculated by applying Paredu measurement method. The variation rates of the Earth magnetic ramp ($\frac{\delta B}{B_0}$) as function of Paredu Mach number M_P is shown in Figure 30.

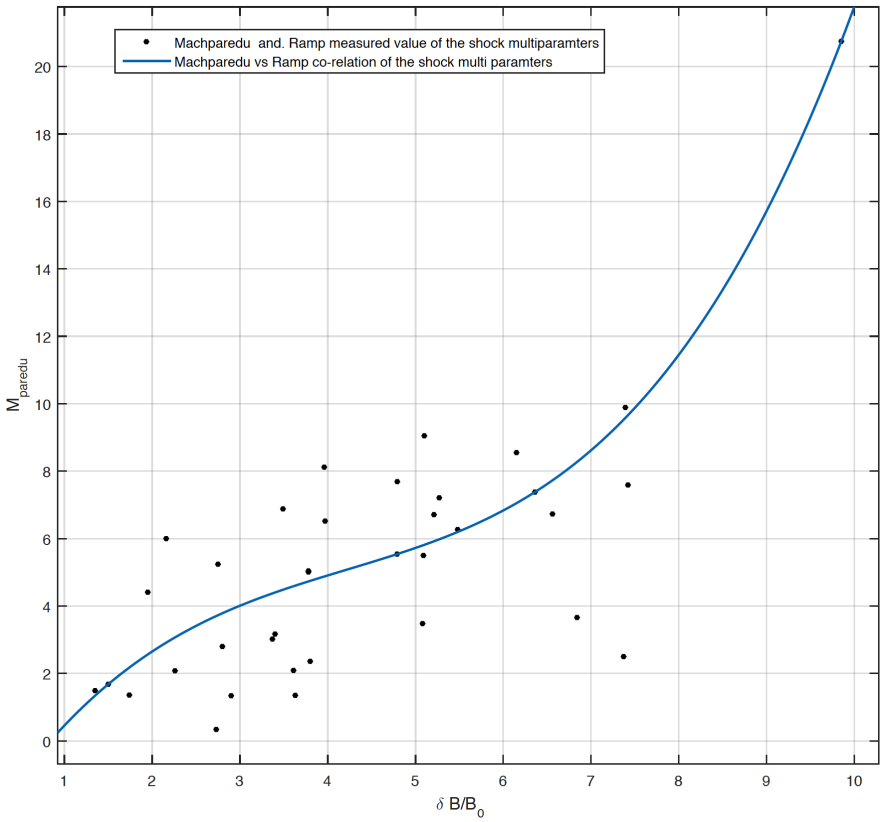

Figure 28: Black dots represents the magnetic ramp variation $\frac{\delta B}{B_0}$

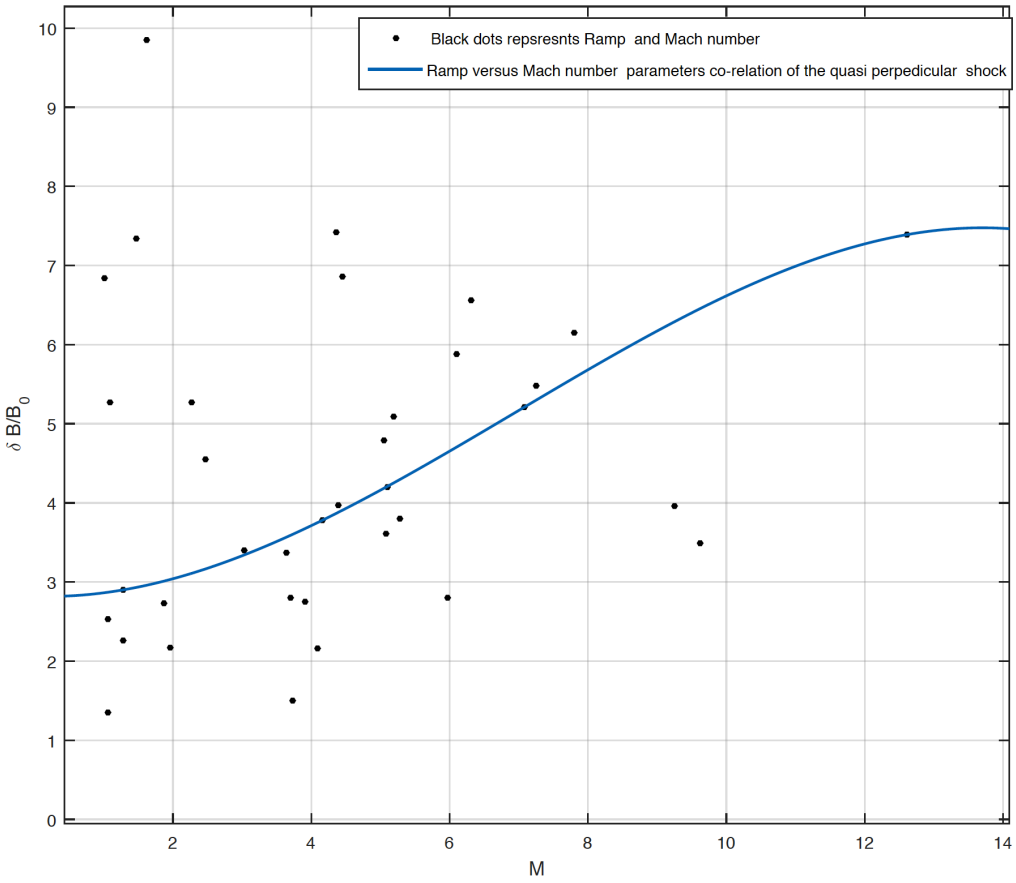

Figure 29: Dependance of magnetic ramp $\frac{\delta B}{B_0}$) on Mach number (M). The blue plot line corresponds to the fitting by polynomial function.

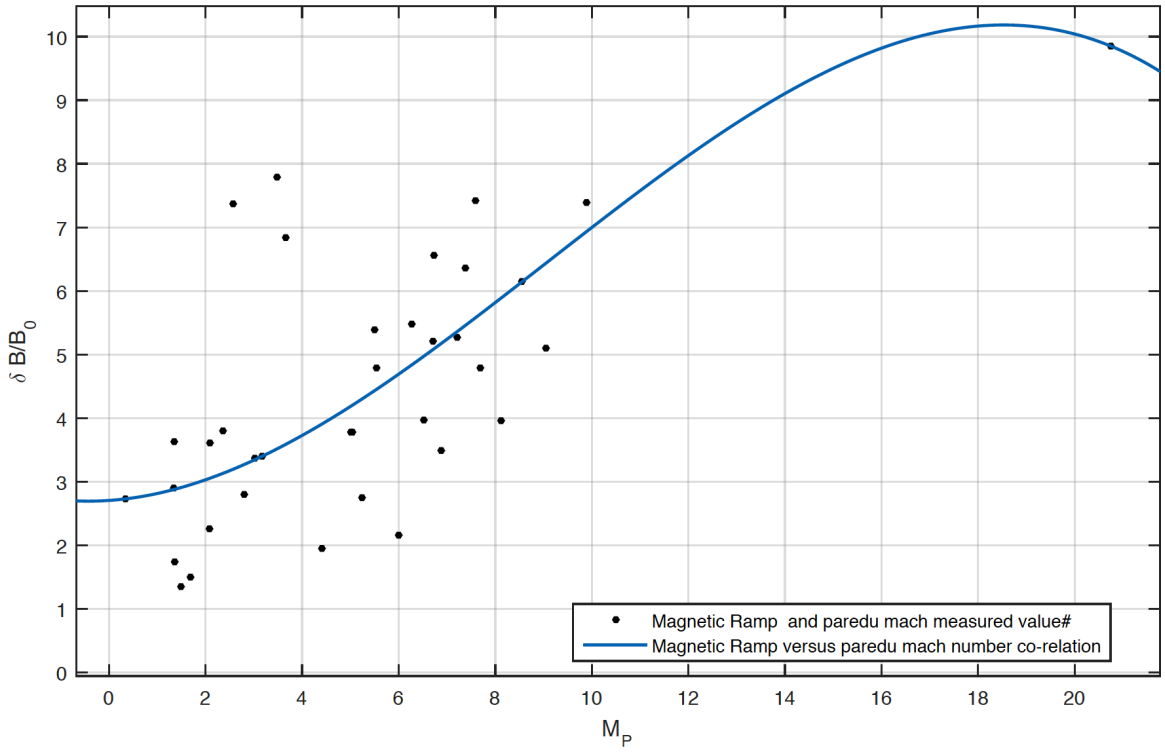

Figure 30: Magnetic ramp $\frac{\delta B}{B_0}$ as a function of Paredu Mach number M_P at low plasma β.

Table 2: Mach number(M),Magnetic ramp value $\frac{\delta B}{B_0}$, upstream magnetic field to shock normal angle (θ_{Bn}), Paredu Mach number(M_P), electron plasma particles density n_e measured at QPS.

No	dd:mm:yy	Start Time	End Time	M	$\frac{\delta B}{B_0}$	θ_{Bn}	M_P	n_e
1	16:02:2015	11:08:00	11:13:00	6.1	5.88	87.15	3.48	23.5
2	05:12:2014	03:05:00	03:40:00	1.28	2.26	45	2.08	10.04
3	27:11:2014	04:05:00	04:15:00	3.7	2.53	86.8	3.16	10.18
4	11:01:2014	22:51‘:00	22:56:00	5.1	4.2	60.92	9.16	7.87
5	26:05:2013	03:45:00	03:47:00	1.87	2.73	80.35	0.33	7.28
6	16:05:2013	03:52:00	03:54:00	5.05	4.79	85.6	9.16	7.28
7	02:06:2012	16:36:00	18:38:00	3.03	3.4	79.7	3.17	5.18
8	01:03:2012	03:13:00	03:17:00	9.25	3.96	81.64	8.12	17.34
9	01:03:2012	03:18:00	03:24:00	7.25	5.48	82.27	6.34	6.38
10	24:01:2012	03:58:00	04:00:00	2.27	5.27	68.51	2.93	27.4
11	01:03:2012	03:25:00	03:31:00	1.47	7.34	46.16	2.14	13.8
12	01:03:2012	03:42:00	03:47:00	5.19	5.09	89.4	5.46	5.31
13	30:12:2011	03:03:45	03:05:00	3.64	3.37	73.97	3.03	9.7
14	30:12:2011	04:21:00	04:26:00	4.11	7.42	80.04	7.6	30.31
15	30:03:2011	14:21:00	14:24:20	1.06	1.35	39.2	1.49	3.82
16	15:02:2011	09:18:20	09:23:00	4.45	6.86	85.5	10.12	5.59
17	27:05:2010	02:28:00	02:33:00	4.16	3.78	56.86	5.08	5.49
18	25:05:2010	05:16:40	05:18:40	9.62	3.49	77.6	6.87	18.63
19	21:01:2010	08:37:00	08:39:00	7.8	6.15	86.66	8.54	12.37
20	20:05:2009	20:16:30	20:18:30	3.91	2.75	85.92	5.24	29.94
21	07:06:2008	12:16:30	12:17:40	12.61	7.39	75.92	9.9	6.59
22	02:06:2007	07:07:00	07:09:00	5.28	3.8	82.99	2.36	8.96
23	7:05:2007	08:27:00	08:29:00	7.08	5.1	83.6	9.06	25.49
24	28:04:2006	05:48:00	05:52:00	5.97	5.21	51.2	6.72	10.89
25	20:04:2005	05:05:00	05:07:00	3.73	2.8	66.17	2.8	26.52
26	04:04:2004	08:57:00	09:02:00	1.28	2.9	61.3	1.69	2.79
27	12:06:2003	06:05:00	06:07:00	1.01	2.9	49.59	1.35	4.7
28	23:05:2002	01:15:00	01:20:00	4.09	6.84	78.2	3.66	19.2
29	20:05:2002	03:40:00	03:45:00	4.39	3.97	54.1	5.99	20.58
30	20:05 :2002	03:40:00	03:45:00	1.96	2.17	54.73	2.67	20.58
31	03:05:2002	08:10:00	08:15:00	6.31	3.97	72.95	6.74	4.08
32	17:01:2001	06:33:00	06:36:00	1.06	2.58	88.01	6.72	12.15
33	17:01:2001	06:33:00	06:36:00	2.47	4.55	87.5	0.57	12.15

6.3 Earth magnetic ramp and variation of the angle between shock normal and upstream magnetic field

The magnetic ramp ($\frac{\delta B}{B_0}$) as a function of the angle variation between shock normal and upstream magnetic field within finite range $45 \leq \theta_{Bn} \leq 90$ is shown as blue curve in Figure 31. Magnetic ramp ($\frac{\delta B}{B_0}$) is a function of the Paredu upstream magnetic field to shock normal angle θ_{BnP} at low plasma $\beta \simeq 0.1$ known as multi-parameters of the QPS proxy correlation validates a real time precise positioning measured value of magnetic ramp and theoretically Paredu upstream magnetic field to shock normal angle θ_{BnP} measured value at low plasma $\beta \simeq 0.1$. Magnetic ramp as a function of the angle variation between shock normal and upstream magnetic field within finite range $45 \leq \theta_{Bn} \leq 90$ known as multi-parameters of the QPS proxy correlation validated with real time measured values.

Un-equipartition ion thermal $T_{\parallel}$ and electron plasma thermal $T_{e\perp}$ energy distribution occurs into magnetic ramp transition region in QPS front with each angle variation between shock normal and upstream magnetic field θ_{Bn} in sunward side $10.05R_E$ compress earth magnetopause resistive magnetic field line boundary surface layer transition region. Two approximation known as bi-Maxwellian approximation and Debye approximation used to predict thermal energy variation rates in ramp region at QPS front. An ions-ions and ions-electrons energy scattering occurs in to the earth magnetic ramp front. Energy-time spectrogram real time precise positioning measurement system detects thermal ions power spectral energy density and upstream electron plasma particles power spectral energy density variation into the earth magnetic ramp transition region at QPS transition time.

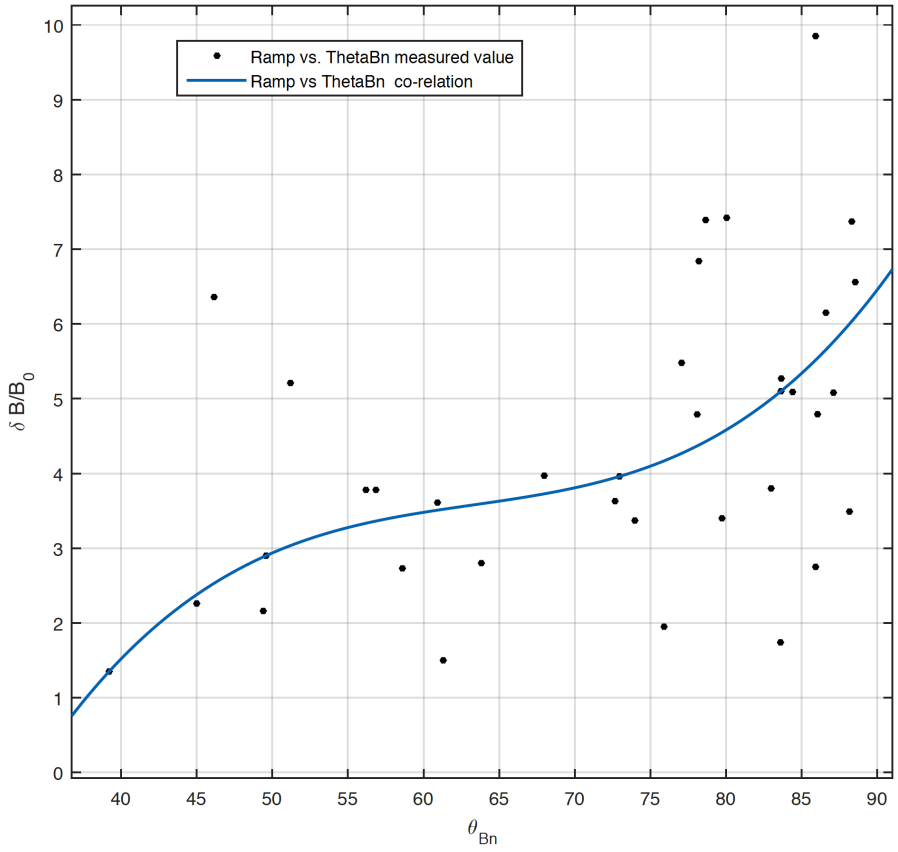

Figure 31: Magnetic ramp ($\frac{\delta B}{B_0}$) as function of the angle variation between shock normal and upstream magnetic field (θ_{Bn}) within discrete range of the $45 \leq \theta_{Bn} \leq 90$) at low plasma β. QPS multi parameters measured value co-relation is validated with Paredu model within 2001-2015.

Table 3: Measured Collisionless QPS parameters

No	dd:mm:yy	Start Time	End Time	M	$\frac{\delta B}{B_0}$	θ_{Bn}	M_P	θ_{BnP}	v_n	$\|B\|$	n_e	v_A	
1	16:02:2015	11:08:00	11:13:00	5.2	3.89	59.35	4.22	63.1	238.8	8.7	23.5	42.2	
2	05:12:2014	03:05:00	03:40:00	1.28	2.26	45	2.08	52.1	176.9	21.75	10.04	147	
3	27:11:2014	04:05:00	04:15:00	3.7	2.53	86.8	3.16	81.74	529.2	28.48	17.56	148.9	
4	11:01:2014	22:51:00	22:56:00	5.1	4.2	60.92	9.16	71.56	272.3	6.89	7.87	53.6	
5	26:05:2013	08:45:00	08:47:00	1.87	2.73	80.35	0.34	52.34	91.79	10.93	7.28	69.6	
6	16:05:2013	03:52:00	03:54:00	8.33	4.79	86.05	7.69	88.6	207.08	6.28	15.2	24.9	
7	02:06:2012	16:36:00	16:38:00	3.03	3.4	79.7	3.17	83.48	216.8	7.45	5.18	71.5	
8	01:03:2012	03:13:00	03:17:00	9.25	3.96	81.64	8.12	81.64	327.8	7.04	17.34	36.8	
9	01:03:2012	03:18:00	03:24:00	7.25	5.48	82.274	6.34	86.89	364.9	6.94	6.38	59.9	
10	24:01:2012	03:58:00	04:00:00	3.11	5.27	83.65	7.27	74.91	88.34	6.74	27.4	28.3	
11	24:01:2012	03:58:00	04:00:0	3.11	5.27	68.5	2.94	74.34	88.14	6.79	27.4	28.3	
12	01:03:2012	03:25:00	03:31:00	3.47	7.34	46.16	2.4	87.99	199.28	8.31	13.6	49.1	
13	01:03:2012	03:42:00	03:47:00	5.19	5.09	89.4	5.46	84.21	411.3	8.06	5.31	76.4	
14	30:12:2011	03:03:45	03:05:00	3.64	3.37	73.97	3.03	87.64	226.3	8.25	9.7	57.8	
15	30:12:2012	04:21:00	04:26:00	4.11	7.42	80.04	7.6	88.21	124.9	7.52	30.31	29.3	
17	30:03:2011	14:21:00	14:24:20	1.06	1.35	39.2	1.49	52.46	158.87	13.52	3.82	150.7	
18	15:02:2011	09:18:00	09:23:00	4.45	6.85	85.5	10.12	44	422.74	6.72	5.59	61.9	
19	27:05:2010	02:28:00	02:33:00	4.16	3.78	56.86	5.08	63.63	100.9	5.42	5.49	50.4	
20	25:05:2010	05:16:00	05:18:00	9.62	3.49	77.6	6.87	86.19	195.23	4.42	18.63	22.3	
21	21:01:2010	08:37:00	08:39:00	7.8	6.15	86.66	8.54	88.78	190.25	3.92	12.73	24.3	
22	20:05:2009	20:16:30	20:18:30	3.91	2.75	85.92	5.24	89.6	119.25	7.6	29.94	30.4	
23	07:06:2008	12:16:30	12:17:40	12.61	7.39	75.92	9.9	66.07	404.2	3.7	6.59	31.4	
24	02:06:2007	07:07:00	07:09:00	5.27	3.8	82.99	2.36	76.8	231.4	6.02	8.96	43.9	
25	07:05:2007	08:27:00	08:29:00	7.08	5.1	83.6	9.06	39.94	181.4	5.93	25.49	39.9	
26	28:04:2006	05:48:00	05:52:00	5.97	5.21	51.2	6.72	69.46	307.29	7.79	10.89	51.5	
27	20:04:2005	05:05:00	05:07:00	3.73	2.8	66.17	2.8	78.76	233.15	13.54	4.7	138.5	
28	04:04:2004	08:57:00	09:02:00	1.28	2.9	61.3	1.69	54.3	237.4	14.17	2.79	147	
29	12:06:2003	06:05:00	06:07:00	1.01	2.9	49.59	1.35	57.2	138.5	13.78	4.7	139.5	
30	23:05:2002	01:15:00	01:20:00	4.09	6.84	78.2	3.86	68.9	136.46	6.7	19.2	33.4	
31	14:05:2003	03:28:00	03:33:00	7.27	1.74	83.6	1.36	88.52	226.45	8.43	2	129	
32	03:05:2002	08:10:00	08:15:00	6.31	3.97	72.95	6.24	85.24	230	5.79	10.58	38.8	
33	20:05:2002	03:40:00	03:45:00	1.96	2.17	54.73	2.67	57.8	230	5.79	10.58	38.8	
34	17:01:2001	06:33:00	06:36:00	5.69	6.56	88.01	6.72	83.83	262.16	7.37	12.15	46.1	
35	17:01:2001	06:33:00	06:36:00	2.47	4.55	87.5	0.57	83.0	262.16	7.37	12.15	46.1	

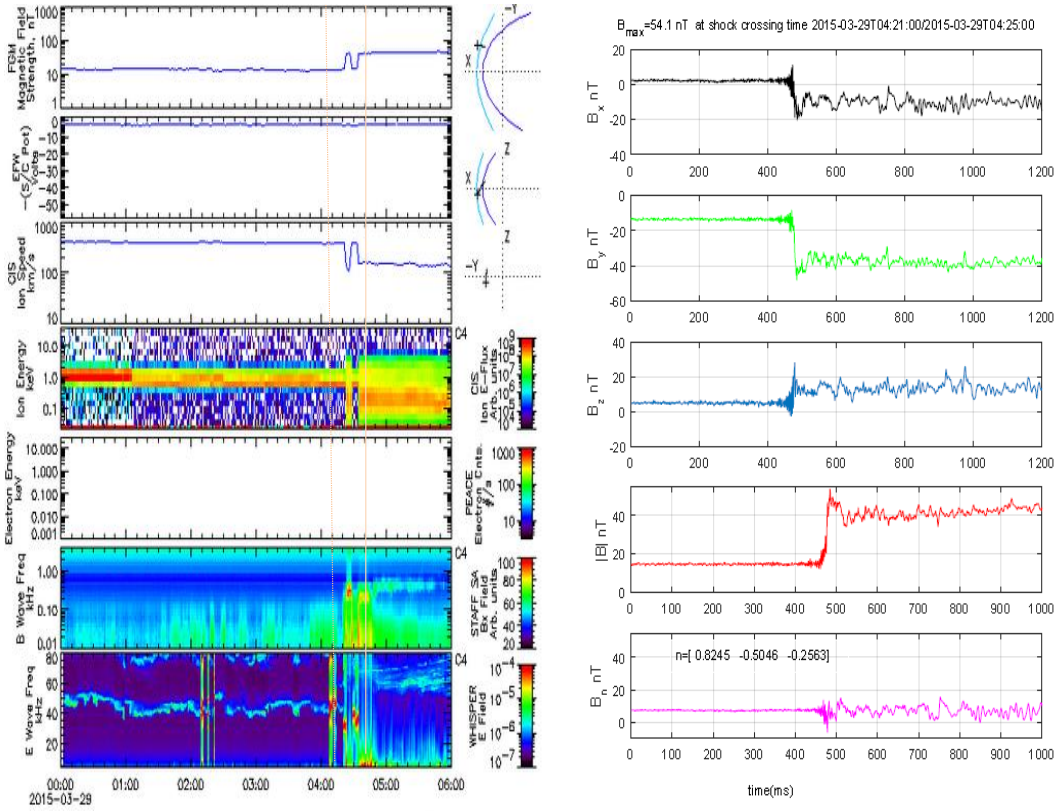

Figure 32: QPS detected at 2015-03-29 T04:21:00UT.

6.4 Summary

The obtained correlation of QPS multi parameters classified as variation rate of the angle between shock normal and upstream magnetic field as a function of the Paredu Mach number M_P at low plasma $\beta \simeq 0.1$ as shown in Figure 26. The magnetic field variation at the QPS magnetic ramp as a function of the Mach number (M) correlation are shown in Figure 29. Magnetic ramp as a function of the Paredu Mach number M_P are shown in Figure 30. This correlation validate the real time measured value of the magnetic ramp as function of the Mach number (M) probabilistic correlation classification evaluated within QPS transition finite time scale. QPS multi parameters correlation classified as magnetic ramp measured value variation rates correlated to the variation rate of the angle between shock normal and upstream magnetic field within finite range $45 \leq \theta_{Bn} \leq 90$ at low plasma $\beta \simeq 0.1$ evaluated at several different times in between 2001-2015 as shown in Figure 31. Precise positioning real time QPS multi-parameters measured value listed in Table 1. Magnetic strength variation in QPS front magnetic ramp at resistive magnetic field boundary surface co-related to each angle between shock normal and upstream magnetic field are shown in Figure 10.

Table 4: Measured value multi-parameters of the QPS

No	dd:mm:yy	Start Time	End Time	M	$\frac{\delta B}{B_0}$ nT	θ_{Bn}	M_p	θ_{BnP}	n_e
1	16:02:2015	11:08:00	11:13:00	6.1	5.08	87.1	4.22	63.1	23.5
2	05:12:2014	03:05:00	03:40:00	1.28	2.26	45	2.08	52.1	10.01
3	03:06:2014	01:59:00	02:06:00	1.29	7.2	81.1	0.1	80.4	5.5
4	11:01:2014	22:51:00	22:56:00	5.08	3.6	60.92	2.09	71.56	7.87
5	26:05:2013	03:45:00	03:47:00	2.51	2.73	45.48	0.35	52.34	7.28
6	16:05:2013	03:52:00	03:54:00	6.41	4.79	78.09	5.54	87.99	15.2
7	02:06:2012	16:36:00	16:38:00	3.03	3.4	79.7	3.17	83.48	5.13
8	01:03:2012	03:13:00	03:17:00	9.05	3.96	85.54	8.24	81.64	17.38
9	01:03:2012	03:16:00	03:17:00	9.25	3.96	81.59	8.12	86.89	6.38
10	01:03:2012	03:18:00	03:24:00	7.25	5.48	82.27	6.34	86.89	6.38
11	01:03:2012	03:25:00	03:31:00	4.72	7.37	80.4	2.75	87.88	13.6
12	01:03:2012	03:25:00	03:31:00	1.47	7.37	46.16	2.14	88.0	13.6
13	01:03:2012	03:42:00	03:47:00	5.39	5.09	84.4	5.5	84.21	5.31
14	24:01:2012	03:58:00	04:00:00	2.28	5.27	68.51	2.94	74.34	5.31
15	30:12:2011	03:03:45	03:05:00	3.64	3.37	73.97	3.02	88.21	26.35
16	30:12:2011	04:21:00	04:26:00	4.12	7.42	80.04	7.59	88.21	1.98
17	15:02:2011	09:18:20	09:23:20	6.33	6.36	52.41	7.91	44.0	5.59
18	15:02:2011	09:18:20	09:23:20	6.83	6.86	46.15	7.38	45.0	12.16
19	27:05:2010	02:27:00	02:33:00	2	3.78	56.19	5.04	58.65	5.29
20	27:05:2010	02:28:00	02:33:00	4.16	3.78	56.85	5	63.63	6.29
21	25:05:2010	05:16:40	05:18:40	7.82	3.49	81.76	5.74	88.19	12.6
22	25:05:2010	05:16:40	05:18:40	9.63	3.49	77.69	6.87	88.2	18.63
23	21:01:2010	08:32:00	08:39:00	7.84	6.15	86.65	8.55	88.76	12.37
24	20:05:2009	20:16:30	20:18:30	3.92	2.75	85.92	5.24	89.6	29.9
25	07:05:2008	12:16:30	12:17:40	12.87	7.39	78.65	9.89	66.07	6.59
26	04:03:2008	03:57:00	04:01:00	16.2	9.85	72.42	18.42	82.69	3.12
27	02:06:2007	07:07:00	07:09:00	5.27	3.8	82.98	2.36	76.8	8.96
28	07:05:2007	08:27:00	08:29:00	7.08	5.1	83.6	9.05	39.94	25.49
29	28:04:2006	05:48:00	05:52:00	5.97	5.21	51.2	6.71	69.46	6.26
30	20:04:2005	05:05:00	05:07:00	4.06	2.8	63.82	2.8	78.76	26.56
31	04:04:2004	08:57:00	09:02:00	1.283	1.5	61.3	1.68	64.3	2.79
32	12:06:2003	06:05:00	06:07:00	1.0	2.9	49.59	1.34	57.2	4.7
33	23:05:2003	01:15:00	01:20:00	4.08	6.84	78.2	3.66	68.9	19.2
34	20:05:2002	03:40:00	03:45:00	5.93	2.16	49.4	6.0	57.8	10.58
35	03:05:2002	08:10:00	08:15:00	4.57	3.97	67.98	6.51	82.24	4.08
36	17:01:2001	06:33:00	06:36:00	5.69	6.56	88.54	6.73	83.83	12.15

6.5 Conclusion

In this work I obtained the an important dependence of magnetic field variation at the front of QPS as a function of Mach number (M) and angle between the normal to the shock ramp and upstream magnetic field (θ_{Bn}). QPS crossing time and shock normal variation was measured at sunward side of Earth at radial distance 10.05 R_E. All QPS measurements validated with theoretical Paredu model. Magnetic field variation in QPS magnetic ramp were correlated with Mach number for each angle between shock normal and upstream magnetic field θ_{Bn} (see e.g. Figure 29).

Also, I analysed QPS parameters which are known as a variation of the angle between shock normal and upstream magnetic field within $45 \leq \theta_{Bn} \leq 90$ at the ramp $\frac{\delta B}{B_0}$ of transition region between 2001-2015 and magnetic strength $|B|$ variation in ramp region of QPS front as a function of the Mach number (M) within Earth bow shock to magnetopause magnetic field transition region. PPSNS real time QPS parameters measured values at several different times between 2001- 2015 are listed in Table 4.

7 Reference list

References

Anderson, K. A., Energetic particles in earth magnetic field, Annual Review, Nuclear Science, *16*, 291-344, 1966

Alexandrova, O., Mangeney, A., Maksimovic, M., Cornilleau, W. N., Bosqued, J., Andre, M., Alfvén vortex filamentary observation in mangetosheath downstream of the quasi perpendicular bow shock, Journal of Geophysical Research, *111*, A12208, 2006

Balikhin, M. A., Nozdrachev, M., Dunlop, M., et al. Observation of the terrestrial

bow shock in quasi-electrostatic subshock regime, Journal of Geophysical Research, (Space Physics), *107*, 1155, 2002

Balikhin, M. A., Pokhotelov, O. A., Walker, S. N., Andre, M., Identification of low frequency waves in the vicinity of the terrestrial bow shock,Planetary and Space Science, *51*, 693-702, 2003

Balikhin, M. A., Pokhotelov, O. A., Walker, S. N., Andre, M., Minimum Variance Free Wave identification; Application to cluster Electrical field data in Magnetosheath, Geophysical Research Letters, *30*, 10,1508, 2003

Balikhin, M. A., Runov, A., Walker1, S. N., Gedalin, M., Dandouras, I., Hobara6, S. , Y., Fazakerley, A., On the fine structure of depolarisation fronts Journal of Geophysical Research, Space Physics, *10.1002*, JA019908, 2014

Balikhin, M., et.al, Observation of chorus waves by the Van Allen Probes: Dependence on solar wind parameters and scale size, Journal of Geophysical Research, Space Physics, 121, 7608–7621 ,2016

Bale, S. D., Mozer, F. S., Horbury, T. S., Density-Transition scale at quasi perpendicular collisionless shocks, Physical Review Letters, *91*, 26, 5004, 2003

Browning, P. K., Book Review, Introduction to plasma physics with space and laboratory applications, Plasma physics and controlled fusion, *47*, 1109, 2005

Bale, S. D., Balikhin, M. A., Horbury, T. S., Krasnoselskikh, V. V., Kucharek, H., Mobius, E., Walker, S. N., Balogh, A., Burgess, D., Lemb‘ege, B., Lucek, E. A., Scholer, M., Schwartz, S. J., Thomsen, M. F., Quasi-perpendicular shock structure and process, Space Science Reviews, *118*, 1-4 ,161-203, 2005

Burch, J. L., Torbert, R. B., Phan, T. D., Electron-scale measurements of magnetic re-connection in space, Science, *352*, 6290, 2016

Burton, R., Christopher, K., Russel, C. T., Alfvén velocity in magnetosphere and its relation to ELF Emission, Journal of Geophysical Research, *75*, 5582-580, 1970

Bengt, U. O., Sonnerup, M., S., D. C., Hanover, NH, U.S.A., Minimum and Maximum Variance Analysis, pp-185-219 , Analysis Methods for Multi-Spacecraft Data Glotz Paschmann and Patrick W. Daly (Eds.), ISSI Scientific Report SR-001, *1.1*, 1998-2000, ISSI/ESA

Caprioli, D., Spitkovsky, A., Cosmic ray induced filamentation instability in collisionless shocks, The Astrophysical Journal Letters, *765:L20*, 8, 2013

Carolus, J. S., George, L., Fundamental of planatory magnetosphere, LMATC, Palo Alto, CA, USA, 2009

Dimmock, A. P., Balikhin, M. A., Walker, S. N., Pope, S. A., Dispersion of low frequency plasma waves upstream of the Quasi-Perpendicular terrestrial bow shock, Annales Geophysicae, *31*, 8, pp. 1387-1385, 2013

Draine, B. T., Bruce T., Bertoldi, Frank Structure of Stationary Photo dissociation Fronts, Astrophysical Journal, *468*, 269.,1996

Edmision, J. P., Kennel, C. F., A parametric survey of the first critical Mach number for a fast MHD shock, Journal of Plasma Physics, *32*,3, pp.429-441, 1984,

Erkaev, N. V., Biernat, H. K. ,Farrugia, C. J. , Computational Methods and Algorithms, Methods of Magnetosphere and Near Space Problems, Russian academy of science, Krasnoyarsk, Russia, 04-04-08, 2013

Foster, J., C., Wygant, J., R., Hudson, M., K., Boyd, A., J., Baker, D., N., Erickson, P., J., Spence , H. E., Shock-induced prompt relativistic electron acceleration in the inner magnetosphere, Journal of Geophysical Research, Space Physics, *120*, 1661-1674, 2015

Fu, H. S., Khotyaintsev, YU. V., Vaivads, A., Retino, A., Andre, M., Energetic electron acceleration by unsteady magnetic re-connection, Nature Physics, *9*, 426- 430, 2013

Fujimoto, M., Phan, T. D., Toth, G., What Controls the Structure and Dynamics of Earths Magnetosphere, Space Science Reviews, *188*, 1, pp 251-286, 2015

Farris, M. H., Russel, C. T., Magnetic structure of the low beta quasi-perpendicular shock, Journal of Geophysical Research, *98*, no.A9, pp 15, 285-15, 294, 1993

Hobara, Y., Balikhin, M., Krasnoselskikh, V., Gedalin, M., Yamagishi, H., Statistical study of the quasi-perpendicular shock ramp widths, Journal of Geophysical Research Atmospheres, *115*, A11, 2010.

Hu, Q., Bengt, U. O. Sonnerup, Reconstruction of 2D structures in the magnetopause. Method improvements, Journal of Geophysical Research Atmospheres, *108*, A1, 2003

Jackson ,A., Spherical shell numerical dynamo benchmark with pseudo-vacuum magnetic boundary conditions, Geophysical Journal International, 196, 2014

Lavraud, B., Borovsky, J. E., Ridley, A. J., Pogue, E. W., Thomsen, M. F., Fazakerley, A. N., Lucek, E. A., Strong bulk plasma acceleration in Earths Magnetosheath, Journal of Geophysical Research, *34*, L 14102,2007

Kajita, T., Atmospheric neutrinos and discovery of neutrino oscillations, Proc. Jpn. Acad. Ser. B, *86*, 303-321, 2010

Kozlov, D. A., Leonovich, A. S., Cao, J. B., The Structure of standing Alfvén waves in a dipole magnetosphere with moving plasma, Annales Geophysicae, *24*, 263-274, 2006

Krasnoselskikh, V., Balikhin, M., Walker, S. N., Schwartz, S., Sundkvist, D., Lobzin, V., Gedalin, M., Bale, S. D., Mozer, F., Soucek, J., Hobara, Y., Comisel, H., The Dynamic Quasi Perpendicular Shock, Cluster Discoveries, Space Science Review, *178*, 535-598, 2013

Machin, G., Engertb, J., Gavioso, R. M., Summary of achievements of the European Metrology Research Programme Project Implementing the new Kelvin, Elsevier, *94*, 149-156, 2016

Machin, G., Bilateral Comparison between NPL and INMETRO Using a High-Temperature Fixed Point of Unknown Temperature, Int. and Thermophys., *36*, 168-179, 2015

Marcowith, A., Bret, A., Bylov, A., The microphysics of collisionless shock waves, Astro physics -HE, arxiv*1604-00318v1*, 2016

Matsukiyo, S., Scholer, M., Dynamics of energetic electrons in nonstationary quasi-perpendicular shocks, Journal of Geophysical Research, Space Physics, *117*, A11015, 2012.

Merka, J., Szabo, A., Sfrankova, J., Nemecek, Z., Earth's bow shock and magnetopause in the case of a field-aligned upstream flow Observation and model comparison, Journal of Geophysical Research, Atmospheres, *108* A7, 2003

Mozer, F. S., Sundkvist, D., Electron Heating in Quasi-Perpendicular Shocks, Journal of Geophysical Research, 2013

Ḿorner, Nils-Axel, Solar Wind, Earth Rotation and Changes in Terrestrial climate, Physical review and research international 3(2):117-136, Geophysics and geodynamics, Rosundavagen, *17* ,13336 saltsj́obaden, Sweeden, 2013

Oka, M., Saito, Y., Mukai, T., Terasawa, T., Field-aligned beam observations at the quasi-perpendicular bow shock: Generation and shock angle dependence, Journal of Geophysical Research, *110*, A05101, 2005

Parker, E. N., in Magntosphere Current system, Geophysical Monograph Series, American Geophysical Union, *118*, 2000

Petrukovich, A., Artemyev, A., Vasko, I. et al., Current Sheets in the Earth Magnetotail, Plasma and Magnetic Field Structure with Cluster Project Observations, Space Science Review, *188* 311, 2015

Russell, R. T., Outer planet magnetospheres,magnetized plasma interaction, solar wind flow to obstacle, Advance in Space Research, *33*, 11, 2004

Russell, C. T., Sudden Compression of the Outer Magnetosphere Associated with an Ionospheric Mass Ejection, Geophysical Research Letter, *26*, 15, 23430-2346, 1999

Russell, C. T., Huddleston, D. E., Kivelson, M., G., et al., Location and shape of the Jovian magnetopause and bow shock, Journal of Geophysical Research, *103*, 082, 1998a

Russell, C. T., Solar wind interaction with the earth magnetosphere, Geophysical Research letter, IEEE Transactions on Plasma Science *14*, 234,1998

Russell, C. T., Lu, G., Luhmann, J. G., Lessons from the ring current injection during the September 24-25,1998 storm, Journal of Geophysical Research, *27*, 9, 2000

Russell, C. T., Journal of Atmospheric and Solar-Terrestrial Physics, *69*,1739, 2007

Russell, C. T., Anderso, B. J., Baumjohann, W., Bromund, K. R., Dearborn, D., The Magnetospheric Multiscale Magnetometers, Space Science Review, *199*, 256, 2016

Russell, C., T.,Burch, L. J., Johlander , A., Rippled Quasi perpendicular Shock Observed by the Magnetospheric Multi-scale Spacecraft, Physical Review Letters, No:*117*, 165101, 2016a

Sironi, L., Spitkovsky, A., Synthetic Spectra from Particle-In-Cell Simulations of Relativistic Collisionless Shocks, The Astrophysical Journal Letters, *92*, 707, 2009

Spitkovsky, A., Chen, P., Laser shaping and optimization of the laser-plasma interaction, AIP, *183*, 569, 2001

Sizov, F., Rogalski, A., Progress in Quantum Electronics, Elsevier, *34*, 278-347, 2010

Stone, R., Tsurutani, T., Collisionless shocks in the Heliosphere, Geophysical Monograph, *34*, 1995

Stone, R., Tsurutani, C. T. ,Some basic concep of the wave-particles interaction, American Geophysical Union, Reviews of Geophysics, *35*, 491-502, 1997

Takaya, I., Nabutada, I., Nakaswka, Compensation of time-variable magnetic moments for a precise attitude control in nano-and micro-satellite mission, Advances in Space Research, *48*, 3, 432-440, 2011

Totorica, S. R., Abel, T., Fiuza , F., Particle acceleration in laser-driven magnetic reconnection, Physics of Plasmas *24*, 041 408, 2017

Treumann, R. A., Jaroschek,C., H., Fundamentals of Non-relativistic Collisionless Shock. Quasi-Perpendicular Supercritical Shocks, Astrophysics Journal, 805, 2181, 2008

Walker, S. N., Demekhov, A. G., Boardsen, S. A., Ganushkina, N. Y., Balikhin, M. A, Cluster observations of non time continuous magnetosonic waves, Journal of Geophysical Research, Space Physics, *121*, 10, 2016

Wilson, L. B., Koval A., Szabo, A. et al., Observations of electromagnetic whistler precursors at super critical interplanetary shocks, Journal of Geophysical Research, *39*, L08109, 2013

Wilson, L. B., Koval, A., Sibeck, D. G., Szabo, A., Cattell, C. A., Kasper, J. C. Maruca, B. A., Pulupa, M., Salem, C. S., Wilber, M., Shocklets, SLAMS, and field-aligned ion beams in the terrestrial foreshock, Journal of Geophysical Research, Space Physics, *118*, 957-966, 2013

Wilson, L. B., Quantified energy dissipation rates in the terrestrial bow shock, Journal of Geophysical Research, Space Physics, *119*, 8:6455, 2014

Wilson, L. B., Sibeck, D. G., Turnery, D. L., Osmanez, A., Capriolix, D., Angelopoulos V. Low frequency waves in space plasma and upstream of the collisonless shock, American Geophysical Union, *arXiv:1607.02183v*, 2016

Wilson, l. B., Low frequency Whistler waves and shocklets observed at quasi perpendicular inter planetary shocks, Journal of Geophysical Research, *114*, A10106, 2013

Yamakawa, H., Full kinetic simulations of plasma flow interactions with meso and micro scale magnetic dipoles, Physics of Plasmas, 21, 2014

Yamakawa, H., Takahiro, Zushi Small sensor probe for measuring plasma waves in space, Space Science, 67, 127, 2015

7.1 List of Tables

7.2 Abbreviations

7.3 Symbols

Symbols used in the Thesis are listed in the Tables (6)-(8).

Table 5: Abbreviations of the symbolic code

bfNo	symbolic code	Abbreviations	
1	ESA	European Space Agency	
2	NASA	National Agronomics and Space Administration	
3	JAXA	Japan Aerospace Exploration Agency	
3	TDS	Time Division Sampler	
4	ev	Electronvolt	
5	HD	Hydrodynamics shock	
6	CS	Collionless Shock	
7	QPS	Quasi Perpendicular Shock	
8	MHD	Magneto Hydro dynamic wave	
9	R_E	Radius of the Earth	
10	R_M	Magnetic Reynolds number	
11	UT	Universal time	
12	GSE	Geo Sentric Eclipse	
13	CIS	Cluster Ions Spectroscopy	
14	HIA	Hot Ion Analyser	
15	FGM	Fluxgate Magnetometer	
16	nT	Nano Tesla	
16	km	kilometers	
17	ms	Mili second	
18	MK	Million Kelvin	
19	N	Number of measurements	
20	VLF	Vey Low Frequency	
21	FFT	Fast Furrier transformation	
22	R_{MEP}	Earth magnetopause dipole distance	
23	Ω_i	Ions cyclotron frequency	
24	μ_m	Magnetic dipole moment of the Earth	
25	F_L	Lorentz force	
26	F_{mt}	Tension force on cross-sectional area of the magnetotail	
27	F_{mp}	Magnetic pressure force on magnetotail	
28	$PPSNS$	Precise Positioning Satellite Navigation System	
29	PPS	Precise Positioning System	
30	$HIAS$	Hot Ion Analyser Sensor	
31	$FGMS$	FluxGate Magnetometer Sensor	
32	$CISS$	Cluster Ion Spectroscope Sensor	
33	IR	Infrared Sensor	
34	MVA	Minimum Variance Analysis	
35	R_1, R_2, R_3, R_4	Cluster Satellite Separation distance	
36	s_1, s_2, s_3, s_4	Arc Length Scale	
37	C_1, C_2, C_3, C_4	Cluster Satellite	
38	t_n	time scale step	

Table 6: Symbolic parameters. Notation description

No	Parameters	Description of the parameters symbol	
1	B	Magnetic field	
2	B_x	Magnetic field x directional component	
3	B_y	Magnetic field y directional component	
4	B_z	Magnetic field z directional component	
5	B_{am}	Minimum initial magnetic field amplitude	
6	B_{max}	Maximum magnetic field amplitude	
6	$\|B\|$	Average magnetic field strength	
7	$\bar{B}_0$	Cartesian coordinate horizontal unperturbed average initial B-field	
8	δB	Magnetic field gradient	
9	$\frac{\delta B}{\bar{B}_0}$	Magnetic ramp	
10	$B_{\|}$	Parallel B-field component	
11	$B_{\perp}$	Perpendicular magnetic field component	
12	B_n	Shock normal magnetic field	
13	B_{up}	Upstream magnetic field	
14	B_d	Downstream Magnetic field	
15	$\bar{B}_x$	Magnetic field average value in x direction	
16	$\bar{B}_y$	Magnetic field average value in y direction	
17	$\bar{B}_z$	Magnetic field average value in z direction	
18	n_x	Shock normal vector in x direction	
19	n_y	Shock normal vector in y direction	
20	n_z	Shock normal vector in z direction	
21	n	Shock normal vector	
22	v_0	Un-shocked plasma particles bulk velocity	
23	v_x	Electron plasma particles velocity in x direction	
24	v_y	Electron plasma particle velocity in y direction	
25	v_z	Electron particles velocity in z direction	
26	$\bar{v_x}$	electron-plasma particles x directional velocity average value	
27	$\bar{v_y}$	electron-plasma particles y directional velocity average value	
28	$\bar{v_z}$	electron-plasma particles z directional velocity average value	
29	v_n	Shock normal velocity	
30	v_{ith}	Ions plasma particles thermal nth order velocity	
31	v_{phe}	Electron plasma phase velocity	
32	v_{ge}	Group wave velocity	
33	v_{eup}	Election plasma particles upstream velocity	
34	v_A	Alfvén velocity	
35	k	Wave number in wave packet	
36	k_{min}	Minimum k-wave number	
37	k_{max}	Maximum k-wave number	
38	K_e	Kinetic energy	
39	v_{sw}	Solar wind velocity	

Table 7: Notations

No	Parameters	Description of the Symbolic Parameters	
1	V_{sh}	Shock wave velocity	
2	l_1, l_2, , , l_{n-1}, l_n	Magnetic field loop at compress earth magnetopause region	
3	ω_0	Initial Plasma gyration frequency in shock rest frame	
4	ω_{pe}	Kinetic electron plasma charge particles gyro radial frequency	
5	Ω_i	Ions cyclotron frequency	
6	r_0	Plasma particles gyro-radii distance at initially in rest position	
7	r_{el}	kinetic electron plasma charge particles gyro-radii distance	
8	r_{il}	kinetic Ion plasma particles gyro-radii distance	
9	m_e	Electron mass	
10	m_i	Ion mass	
11	μ_0	Magnetic field permeability in vacuum	
12	μ_e	Electron permeability in vacuum	
13	ε_0	Electric field permeability	
14	n_e	Electron plasma charge particles density	
15	n_i	Ions plasma charge particles density	
16	n_0	Maximum solar wind density	
17	P_{ie}	Solar wind ions electron plasma charge particles pressure	
18	P_{ten}	Pressure tension	
19	P_0	Current time solar wind pressure	
20	$P_{i\|\|}$	Ion parallel pressure	
21	$P_{e\perp}$	Electron plasma particles perpendicular pressure	
22	$T_{i\|\|}$	Ions plasma particles parallel temperature	
23	$T_{e\perp}$	Electron plasma particles perpendicular temperature	
24	λ_{De}	Electron plasma particles Debye length scale	
25	$\frac{c}{\omega_{pe}}$	Electron plasma particles inertial scale length	
26	$\frac{c}{\omega_{pi}}$	Ion plasma particles inertial scale length	
27	λ_e	Electron plasma wavelength	
28	λ_{min}	Minimum wavelength of the k-wave number	
29	λ_{max}	Maximum wavelength of the k-wave number	
30	k_{max}	Maximum k-wave number in wave packet	
31	k_{min}	Minimum k-wave number in wave packet	
32	σ	e-plasma particles magnetisation	
33	M_{f1}	First critical Mach number	
34	k_B	Boltzmann constant	
35	P_B	Magnetic field moment of inertia, invariant	
36	P_e	Electron plasma moment of inertia	
37	$-q_e$	Electron plasma particle negative charge	
38	q_i	Ions plasma particles positive charge	
39	θ_{Bn}	Angle between shock normal and Upstream B-field	
40	j_e	Electron plasma shock current	

Table 8: Notation

No	Parameter	Description of the Parameter	
1	E_0	Shock rest position electric field	
2	E_x	Short live electric field in x direction	
3	E_y	Short live electric field in y direction	
4	E_z	Short live electric field in z direction	
5	$\vec{E_x}$	Short live electric field vector in x direction	
6	$\vec{E_y}$	Short live electric field vector in y direction	
7	$\vec{E_z}$	Short live electric field vector in z direction	
8	$\bar{E}$	Average short live inductive electric field	
9	$E_\parallel$	Short live inductive parallel electric field	
10	$E_\perp$	Short live inductive perpendicular electric filed	
11	C	Speed of light	
12	Ψ	Magnetic flux	
13	ψ	Propagating wave phase	
14	γ	Lorentz factor/latent heat constant	
15	P_M	Magnetic field pressure	
16	β	Solar wind thermal pressure to magnetic field pressure ratio	
17	R_{MEP}	Approximate Earth magnetic dipole field distance	
18	R_E	Earth radii	
19	R_M	Magnetic Reynolds number	
20	L_N	Length scale	
22	A_{mt}	Magnetotail cross sectional area	
22	v_0	Shock rest frame initial plasma particles velocity	
23	M_P	Paredu Mach number	
24	θ_{BnP}	Paredu upstream B-field to shock normal angle	
25	k_{int}	intermediate wave wavelength	
26	MMS	Magnetospheric Multiscale Magnetometers	
27	v_μ	electron muon velocity	
28	v_τ	electron tau velocity	
29	v_e	electron nutrino velocity	
30	θ_{Bk}	Angle between wave propagation and Upstream magnetic field	

Table 9: Physical parameters value

No	physical variable parameters contents	physical variable parameters value	
1	e-plasma particles charge $(-q_e)$	$1.62012 \times 10^{-19} C$	
2	Astronomical Unit (AU)	$1.495978707 \times 10^{8} km$	
3	Speed of light(C)	$2.99792458 \times 10^{8} ms^{-1}$	
3	Electron mass(m_e)	$9.1095 \times 10^{-28} gm$	
3	Ion mass (m_i)	$1.672623 \times 10^{-24} gm$	
4	Earth radii (R_E)	6380 km	
5	Electron plasma particles wave length (λ_e)	$2.7 \times 10^{-27} m$	
6	Electron plasma particles Debye length (λ_{De})	meter	
7	Unshock solar wind magnetic field	$10^{-9} tesla$	
8	Electron temperature (T_e)	$10^{5} Kelvin$	
9	Solar wind density (n_0)	$10^{6}\ cm^{-3}$	
10	Photon mass	$3 \times 10^{-27} ev/cm^2$	
11	Electron magnetic moment (P_e)	$9.27400915 \times 10^{-24}$ joules/Tesla	
12	Electron radius upper limit in bonded particles(r_0)	$2.31 \times 10^{-15} M$	
13	Wavelength of photonic light (λ_C)	0.4 up to 7.7 μm	
14	e-shock wave length (λ_e)	10 to 300μm	